

Strength, deformation, and equation of state of tungsten carbide to 66 GPa

B.L. Brugman^{1*}, F. Lin², M. Lv¹, C. Kenney-Benson³, D. Popov³, L. Miyagi², and S.M. Dorfman¹

¹Michigan State University, Dept. of Earth and Environmental Science, East Lansing MI 48824,

²University of Utah, Dept. of Geology & Geophysics, Salt Lake City, UT, 84112

³HPCAT, X-ray Science Division, Argonne National Laboratory, Argonne, IL 60439

*Corresponding Author, now at Arizona State University

E-mail: bbrugman@asu.edu, +1 (517) 355-4626

Abstract

Strength, texture, and equation of state of hexagonal tungsten monocarbide (WC) have been determined under quasi-hydrostatic and non-hydrostatic compression to 66 GPa using angle-dispersive X-ray diffraction in the diamond anvil cell. Quasi-hydrostatic compression in a Ne pressure medium demonstrates that nanocrystalline WC is slightly less incompressible than bulk-scale WC, with respective bulk moduli of $K_0 = 397 \pm 7$ and 377 ± 7 GPa and pressure derivatives $K_0' = 3.7 \pm 0.3$ and 3.8 ± 0.3 . This decrease in incompressibility with grain size is similar to behavior observed in other ceramics. Under nonhydrostatic compression, WC supports a mean differential stress of ~12-15 GPa at plastic yielding, which occurs at ~30 GPa. Strength in WC is anisotropic, with the (001) plane supporting 29-42% higher stress than stresses calculated from mean strain. Simulations using an Elasto-ViscoPlastic Self-Consistent model (EVPSC) indicate that strength inferred from lattice strain theory may be overestimated due to effects of plastic deformation. Plastic deformation generates a texture maximum near $\langle\bar{2}110\rangle$ in the compression orientation, initially through prismatic slip on the $\{10\bar{1}0\}\langle\bar{1}2\bar{1}0\rangle$ and $\{10\bar{1}0\}\langle 0001\rangle$ slip systems, followed by activation of pyramidal slip on $\{10\bar{1}1\}\langle\bar{2}113\rangle$ at ~40-50 GPa.

Keywords: strength, deformation, EOS, ceramics, tungsten carbide

1. Introduction

Tungsten monocarbide is a transition metal carbide used extensively in industrial and research technology because of an abundance of useful physical properties, including high strength and hardness, ultra-incompressibility, wear resistance, and high melting temperature [1–5].

Because of its high strength, synthetic WC is used as a sturdy backing for abrasives on modern industrial cutting tools, in wear-resistant coatings [6–9], and in the manufacture of anvils and support structures in high-pressure apparatuses [1,10, and e.g. 11]. Improving the strength of parts made from WC and extending the pressure range accessible by high-pressure devices are active areas of research [e.g. 12,13]. WC is also one of the least compressible materials known, with a bulk modulus comparable to other incompressible materials such as Os-borides, cBN, and cRuO₂ [7,14–16]. WC has also been useful to high-pressure/temperature redox chemistry: it was originally discovered via reduction of tungsten oxide [17,18], a reaction that defines the WC-WO redox buffer used in geochemistry [19], and also occurs naturally in Earth’s reduced mantle as the rare mineral qusongite [20]. Despite these remarkable properties and widespread applications, the strength and deformation mechanisms of WC under extreme quasi-static stress have not been studied.

Constraints on the equation of state (EOS) of WC are important for understanding its response to extreme conditions and chemistry [21]. Experimental work on WC has reported values of the ambient pressure bulk modulus, K_0 , ranging from 329–452 GPa [2,22] depending on method and grain size of WC. EOS measurements for WC based on X-ray diffraction of samples compressed in a multianvil device under hydrostatic conditions with high-temperature annealing have been reported to 30 GPa [10]. Relative to these measurements, experiments conducted in the diamond anvil cell (DAC) have yielded systematically higher volumes and incompressibility under pressure, possibly due to nonhydrostatic stress. Recent first-principles studies provide values for K_0 for WC that mostly cluster in the center of the experimental range for WC ~380–390 GPa. Additional experiments are needed to reconcile these differences in observed and predicted bulk compression behavior.

Nano-grain-size WC was also suggested to be much more incompressible than bulk-grain-size WC, with K_0 ~452 GPa, similar to diamond [2]. In general, effects of nanoscale grain sizes on bulk incompressibility are not clearly systematic: a few-10s-nm grain size cubic BN [23], Al₂O₃ [24] and TiO₂ [25] have been observed to be less incompressible than bulk samples, while nano-

grain-sized noble metals Au, Ag, and Pt appear more incompressible than micron-scale grain sizes [16,26,27]. For other materials such as Fe, TiC, and TiN, observations suggest that grain sizes have either no effect or nonmonotonic effects on bulk modulus [28–30].

Anisotropic elasticity of WC has also been studied by both experiments and theory, but limited high pressure constraints are available. The elastic stiffness coefficients c_{ij} for WC have been studied at ambient conditions experimentally [31] and computationally [2,8,32–36]. Theoretical c_{ij} s as a function of pressure have been computed to 100 GPa [35,36], and agree well with previous experimental values at ambient conditions, with the exception of c_{13} , which is consistently predicted to be ~100 GPa lower than the experimental value [31]. The pressure-dependence of the c_{ij} s of WC has not been measured experimentally, and experimental tests of theory are required.

The high strength, i.e. maximum stress before transition from elastic to plastic deformation, of WC and other strong metal-light element compounds is linked to covalent bonding which impedes deformation mechanisms common in metals. In hexagonal $P\bar{6}m2$ WC, carbon atoms are positioned as interstitial layers in what would be an otherwise softer (though among the strongest of all metals) hexagonally closest-packed sub-lattice of W atoms [37,38]. This interstitial positioning combined with the density of valence electrons promotes strong covalent W-C bonding [5,38]. In addition, the incomplete $5d$ band in W atoms promotes replacement of the softer metallic W-W bonds by W-C covalent bonds, increasing the hardness and incompressibility of WC relative to WN, which has similar structure but different valence states [33]. The interstitial C atoms also impede the movement of dislocations within the lattice during strain and act to prevent basal slip, which is commonly observed in hexagonal materials [39]. Slip at ambient conditions activates in the closest-packed directions and is prismatic on $\{10\bar{1}0\}\{0001\}$ and $\{10\bar{1}0\}\{2\bar{1}\bar{1}0\}$, and Burgers vector $\langle 2113 \rangle$ has been noted as dislocation decomposition of $\langle 2\bar{1}\bar{1}0 \rangle$ [39,40]. This blocking of common slip systems and dislocation motion in general increase hardness and strength by impeding plasticity [5]. Ultimately, there is still sufficient metallic character such that WC only reaches a

Vickers hardness of ~30 GPa [41,14], making WC harder than many industrial ceramics, but substantially softer than superhard (Vickers hardness > 40 GPa) materials like diamond [e.g. 42] and cubic boron nitride [43,44]. However, at high pressures, the strength, hardness, and slip mechanisms of WC have not been studied. Because the high-pressure compressive yield strength is related to both hardness and bulk modulus, WC is expected to yield at lower stress relative to superhard materials, but comparable or higher stress than yielding in other ultra-incompressible ceramics. Elastic and plastic anisotropy induced by interstitial carbon layers may translate into slip strength anisotropy in the WC lattice.

To characterize the strength, deformation, and the equation of state of WC with pressure, we compressed hexagonal WC powder of bulk (microcrystalline) and nanocrystalline grain size to pressures up to 66 GPa at room temperature with X-ray diffraction in the diamond anvil cell (DAC). Complementary Elasto-ViscoPlastic Self Consistent (EVPSC) simulations on textures and lattice strains were carried out to determine the plastic deformation mechanisms and strength at high pressures consistent with new experimental data. Our results extend the pressure range of the quasi-hydrostatic EOS of WC to 59 and 64 GPa for bulk and nanocrystalline WC, respectively, and offer new constraints on strength and plastic deformation mechanisms of WC.

2. Experimental Details

2.1 Sample Preparation and Loading

Microcrystalline (Alfa Aesar) and nanocrystalline (Inframmat) hexagonal WC powders were used as sample materials. Initial grain sizes of these materials were determined to be 1.2 μm and 54 nm based on Rietveld refinement of ambient X-ray diffraction (XRD) patterns [45] collected using a Bruker DaVinci D8 powder diffractometer with Cu $K\alpha$ source at the Michigan State University Center for Material Characterization.

Volumetric compression under hydrostatic conditions and strain and texture development under non-hydrostatic conditions were investigated in WC in diamond anvil cells. For hydrostatic experiments, WC powder was loaded with Au (internal pressure standard, Alfa Aesar) and ruby

(internal pressure standard used to confirm success of gas loading, ADFAC) within a Ne medium using the COMPRES/GSECARS gas-loading apparatus [46]. Each sample was enclosed by a rhenium gasket pre-indented to $\sim 40\text{-}\mu\text{m}$ thickness with $\sim 150\text{-}\mu\text{m}$ sample chamber and compressed in symmetric DACs with anvils with $300\text{-}\mu\text{m}$ culets. For nonhydrostatic experiments, WC powder was packed without a medium and an Au foil standard was placed on top. An X-ray transparent beryllium gasket pre-indented to $32\text{ }\mu\text{m}$ with a $100\text{-}\mu\text{m}$ -diameter sample chamber hole was used with a 2-pin panoramic DAC with $300\text{-}\mu\text{m}$ anvil culets. Gaskets were machined using the HPCAT laser cutting facility [47]. Samples were compressed in 2-10 GPa steps up to maximum pressure of 66 GPa, with pressure at each step calculated using the equation of state for Au [48].

2.2 X-ray diffraction in the DAC

Upon compression, synchrotron X-ray diffraction was obtained using both axial diffraction geometry in a symmetric DAC in which the X-ray probe was parallel to the loading axis (both grain sizes), and the radial diffraction geometry in a panoramic DAC in which the incident X-rays were perpendicular to the loading axis (bulk WC only). Angle-dispersive X-ray diffraction (ADXRD) was conducted at the High-Pressure Collaborative Access Team (HPCAT) beamline at Argonne National Lab, Sector 16-BM-D. X-rays monochromatized to 40 keV (axial experiments) or 37 keV (radial experiments) were focused to $4\text{-}6\text{-}\mu\text{m}$ spot size using Kirkpatrick-Baez focusing mirrors and collimated using a $90\text{-}\mu\text{m}$ pinhole. Diffraction patterns were collected for 60-80s on a MAR2300 image plate detector. Detector geometry was calibrated using a CeO_2 standard.

Diffraction patterns were masked to eliminate saturated intensity and integrated to 1-D profiles using Fit2D [49] or Dioptas software [50]. For data collected in the axial geometry, diffraction peaks were fit to Voigt lineshapes using the IgorPro MultipeakFit module. For analysis of data collected in the radial geometry, each pattern was divided into 5° azimuthal wedges over the full 360° azimuthal range for full-profile Rietveld refinement with Materials Analysis Using Diffraction (MAUD) software [51,52]. The synchrotron instrument parameters in MAUD were refined using the CeO_2 standard. Sample parameters, including polynomial backgrounds, lattice

constants, grain size, and microstructure were refined at each pressure step. Strain was fit at each step for WC and Au using the “Radial Diffraction in the DAC” model. To include the maximum number of diffraction lines from WC in our calculations and to minimize the effects of peak overlap, Q-values for higher-order parallel planes were fixed equal to the lowest order plane to which they were parallel. Be and BeO phases (at 1 bar) were included in the refinement to model diffraction from the gasket peaks. Texture in all phases was fit using the Entropy-modified Williams-Imhof-Matthies-Vinel (E-WIMV) texture model [53,54] with an imposed fiber symmetry. The orientation distribution function (ODF) was exported from MAUD and inverse pole figures were plotted using the BEARTEX software [55]. Pressure was calculated from unit cell volumes of Au determined by fitting the (111) diffraction peak in the 5° azimuthal wedge containing the hydrostatic angle ($\psi = 54.7^\circ$).

3. Results and Interpretation

Representative diffraction patterns for bulk and nano-crystalline WC compressed in Ne are presented in Fig. 1. All observed diffraction peaks correspond to the WC sample, Ne medium, Au pressure standard, and Re gasket. Ne peaks (highly textured spots) and diamond spots were masked to remove overlap with WC sample. Only non-overlapped WC and Au diffraction lines were used to determine unit cell parameters. Lattice spacings for WC (001, 100, 101, 110, and 111) and Au (111, 200, and 220) were fit by least squares with UnitCell Software [56]. The resulting unit cell volumes for both nano-crystalline WC and bulk WC are presented in Fig. 2.

3.1 Equation of state and linear compressibility

Volume-pressure data collected in the axial geometry for WC compressed in Ne medium (Fig. 2) were fit to a 3rd order Birch-Murnaghan equation of state (BME), yielding EOS parameters tabulated with previous work in Table 1. Previous studies in the DAC report higher K_0 but lower K_0' than calculated in our work or the work by Litasov et al. [10]. Our results use the pressure scale of Dewaele [48], and yield pressures ~3-5% higher pressures than the pressure scales of Mao [57] and Heinz and Jeanloz [58] used by other workers. Adjusting previous results to the Dewaele ruby

scale would increase the apparent disparity in K_0 values. In addition to non-hydrostatic stress and choice of pressure scale, the trade-off between K_0 and K_0' during EOS fitting is responsible for some of the difference between reported values for the EOS parameters (Fig. 3). Combined with independent measurements of elasticity from ultrasonic [1,7] and shock wave [59] studies, the consensus value for K_0 is ~ 380 -400 GPa, which is consistent with our bulk K_0 obtained from the EOS fit, 397(7) GPa when V_0 is fit to 20.76 Å³. The range of K_0' most consistent with our data and the consensus K_0 is ~ 3.6 -4.3. In comparison, density functional theory (DFT) predictions using both the local density approximation (LDA) and generalized gradient approximation (GGA) all predict $K_0' > 4$ [2,8,21,35,36]. When higher values for V_0 are fixed during the EOS fit to high pressure data, we also obtain $K_0' > 4$ consistent within uncertainty with our results (Fig. 3). Our experiments indicate that the bulk modulus of nano-crystalline WC is lower than that of the bulk material, and consistent with the consensus of ultrasonic, shock wave, and DFT EOS.

The ratio of the hexagonal lattice parameters c/a can indicate a convolution of anisotropic elasticity and anisotropic stress. Our experimental values for c/a in bulk WC compressed hydrostatically in Ne medium indicate a systematically lower ratio than other DAC XRD studies that employed nonhydrostatic media (Fig. 4). Again, note that axial XRD in the DAC samples crystallites oriented near the direction of minimum stress. Anisotropic stress combined with anisotropic elasticity will result in systematic differences in lattice parameters c and a calculated from diffraction lines at the minimum stress orientation. Systematically higher c/a ratio from studies of WC under non-hydrostatic compression in the axial geometry indicates anisotropy in linear compressibility. The linear compressibilities χ_a and χ_c may be determined from their relations to the bulk modulus and the pressure dependence of the c/a ratio in a hexagonal material [60,61]:

$$2\chi_a + \chi_c = \frac{1}{K} \quad (1)$$

$$\chi_a - \chi_c = \left(\frac{\partial \ln(c/a)}{\partial P} \right)_T \quad (2)$$

Under hydrostatic conditions, the c/a ratio of WC increases non-linearly with pressure, so the slope of its pressure dependence cannot be accurately represented with a constant value. To determine the pressure dependence of c/a , we determined lattice parameters a and c and $K(P)$ from the quasi-hydrostatic diffraction data, fit a least-squares 3rd order BME to parameters a and c to obtain parameters $a(P)$ and $c(P)$, and computed numerical derivatives of the ratio c/a at each pressure step.

Experiments and theoretical computations agree that the a direction of WC is more compressible than c . Our BME fit of lattice parameters for WC yields linear ambient bulk moduli of $K_a = 366$ GPa and $K_c = 456$ GPa for bulk WC and $K_a = 359$ GPa and $K_c = 407$ GPa for nanocrystalline WC. The value of K_c for nanocrystalline WC compressed in Ne medium is lower than for bulk WC, and lower than the value reported in previous experiments on nanocrystalline WC [2].

3.2 Differential Stress and Elastic Stiffness Coefficients

Without a hydrostatic medium, a sample in an opposed anvil device such as the DAC sustains approximately uniaxial compressive stress, with a maximum stress σ_3 parallel to the direction of the compression by the diamonds, and a radial minimum stress σ_1 [62]. The difference between these stresses is termed the differential stress. In order to characterize the effects of non-hydrostatic stress on deformation of anisotropic materials, the radial diffraction geometry allows observation of strains at a wide range of orientations relative to the orientation of maximum stress. Unrolled radial “cake” patterns obtained at selected pressures upon compression of bulk WC are presented in Fig. 5.

Diffraction lines of WC under anisotropic strain exhibit varying d -spacing along the azimuthal angle. The measured d -spacing d_m deviates from the hydrostatic d -spacing d_p as a function of the angle ψ between the normal vector to the diffracting plane and the loading axis as quantified by the non-hydrostatic lattice strain $Q(hkl)$ for individual lattice planes hkl [63,64]:

$$d_m(hkl) = d_p(hkl)[1 + (1 - 3\cos^2\psi)Q(hkl)]. \quad (3)$$

Our detection limit for $Q(hkl)$ is $\sim 8\text{--}9 \times 10^{-4}$, with typical uncertainty up to $6\text{--}7 \times 10^{-4}$, exemplified by the strain observed in the (201) plane at 16 GPa. For materials in the hexagonal crystal system such as WC, $Q(hkl)$ is a quadratic function [64,63,61] of lattice plane orientation $B(hkl)$, relative to the loading axis:

$$Q(hkl) = m_0 + m_1 B + m_2 B^2, \quad (4)$$

where $B(hkl) = \frac{3a^2 l^2}{[4c^2(h^2+hk+k^2)+3a^2 l^2]}$, in which a and c are the measured lattice parameters at pressure, and the m_i are the coefficients of the quadratic relationship between Q and B .

In the elastic regime, the strain $Q(hkl)$ is a function of the differential stress, t , the elastic shear moduli G_R and G_V under isostress (Reuss bound) and isostrain (Voigt bound) conditions, respectively, and α , a constant between 0.5 and 1 which determines the weight between Voigt and Reuss conditions, i.e. stress vs. strain continuity at grain boundaries [63–65].

$$Q(hkl) = \frac{t}{3} \left[\frac{\alpha}{2G_R(hkl)} + \frac{1-\alpha}{2G_V} \right], \quad (5)$$

The mean strain $\langle Q(hkl) \rangle$ and range of $Q(hkl)$ for different diffraction lines indicate lattice strain due to increasing anisotropic stress, change in anisotropic elasticity, or both. Above the yield stress, in the viscoelastic regime, $Q(hkl)$ will be modified by plasticity as well.

We used full-profile refinement in MAUD (Fig. 5) with the “Radial Diffraction in the DAC” stress model to determine Q -factors for each hkl (Fig. 6). With increasing pressure (and differential stress), $Q(hkl)$ increases for all diffraction lines, and the range of $Q(hkl)$ observed increases, with maximum lattice strain in WC at (001) and (100) directions, and minimum lattice strain near (101) and (112). Up to ~ 30 GPa, strain is increasingly anisotropic for WC (Fig. 6e). At ~ 30 GPa, the effect of pressure on Q tapers off, and anisotropy in Q values is due to both elastic and plastic deformation.

Fig. 7a illustrates the range of differential stress values obtained for analysis assuming Reuss and Voigt bounds. In the Reuss limit ($\alpha = 1$, implying stress continuity across crystallite

boundaries), mean strain $\langle Q(hkl) \rangle$ and prior constraints on the shear modulus G [65] may be used to determine t :

$$t = 6G\langle Q(hkl) \rangle f(x), \quad (6)$$

where $f(x)$ is a function of α and elastic anisotropy factor x . Across a range of materials and crystal systems f has been shown to have a value close to 1 [e.g. 66], so we adopt $f=1$ in analysis of WC. Aggregate shear modulus $G(P)$ was constrained by extrapolation of a linear fit of ultrasonic data obtained up to 14 GPa [in 1]. Based on these assumptions, elastic differential stress sustained by WC is reported in Fig. 10, with error bars computed based on the standard deviation of $Q(hkl)$ at each pressure.

Average values of differential stress obtained from lattice strain increase with pressure throughout the entire range of this study, to a maximum of 27 (Voigt, $\alpha=0$) to 33 (Reuss, $\alpha=1$) GPa at the maximum pressure measured, 66 GPa. The slope of $t(P)$ decreases at ~ 30 GPa, at which pressure the observed differential stress is ~ 12 GPa. A decrease in slope of $t(P)$ is consistent with expected behavior at initiation of plastic flow.

Fig. 7b illustrates Reuss stresses for individual lattice planes in which $t(hkl)$ is calculated using equation 6 with $Q(hkl)$ for (001), (100), (110), (101), and (111) and the X-ray shear modulus $G_R^X(hkl)$, given by [63]:

$$\left[2G_R^X(hkl)^{-1} = \frac{1}{2}(2S_{11} - S_{12} - S_{13}) + B^2(-5S_{11} + S_{12} + 5S_{13} - S_{33} + 3S_{44}) + B^4(3S_{11} - 6S_{13} + 3S_{33} - 3S_{44}) \right], \quad (7)$$

where the S_{ij} are the elastic compliances. Differential stress $t(001)$ is substantially higher than $t(hkl)$ for other planes, supporting 28 GPa of differential stress at the yield stress, 29% higher than the Reuss bound differential stress calculated from $\langle Q(hkl) \rangle$ with theoretical G_R , 42% higher than the differential stress determined from $\langle Q(hkl) \rangle$ and the aggregate shear modulus.

In the elastic regime, the strain anisotropy from $Q(hkl)$ can also be used to compute elastic compliances S_{ij} . S_{ij} at a given pressure may be determined by the vector product of the inverted

coefficient matrix of the lattice strain equations [63] with their solution matrix for the hexagonal system [61,63]:

$$\begin{bmatrix} 2 & -1 & -1 & 0 & 0 \\ -5 & 1 & 5 & -1 & 3 \\ 3 & 0 & -6 & 3 & -3 \\ 1 & 1 & 1 & 0 & 0 \\ 0 & 0 & 2 & 1 & 0 \end{bmatrix}^{-1} \begin{bmatrix} 6m_0/t \\ 6m_1/t \\ 6m_2/t \\ \chi_a \\ \chi_c \end{bmatrix} = \begin{bmatrix} S_{11} \\ S_{12} \\ S_{13} \\ S_{33} \\ S_{44} \end{bmatrix} \quad (8)$$

Equations (1-6 and 8) may thus be used to combine $Q(hkl)$ with independent constraints on the linear incompressibilities in a and c directions χ_a and χ_c derived from hydrostatic data above, and an average $G(P)$ or $t(P)$, to determine S_{ij} s. The elastic stiffness coefficients (c_{ij} s) are obtained from equivalence relations between c_{ij} s and S_{ij} s [67].

Calculated c_{ij} values for the full experimental pressure range are shown in Fig. 8. Note that apparent c_{ij} are modified by convolved effects of plasticity with elasticity on strain behavior. Our experimental c_{ij} are in best agreement with predicted values from DFT [35,36] below the plastic yield pressure at ~ 30 GPa, providing support for the accuracy of these predictions. DFT predicts that all c_{ij} increase with pressure. The relative behavior of c_{12} and c_{13} may indicate a minor correction is needed to DFT predictions. At 16 GPa, our lowest pressure with resolved strain, c_{12} and c_{13} are \sim equivalent, as observed by ultrasonic methods at 1 bar [31], though ultrasonic measurements obtained slightly higher values for both than our high pressure values. Our observations suggest that c_{12} decreases or remains approximately constant with pressure. In contrast, DFT predicts that c_{12} should consistently be significantly greater than c_{13} and should increase faster with pressure than c_{13} . Both experimental studies find that c_{12} is the weakest of the stiffnesses, and the value of c_{12} derived from radial diffraction also may be more likely than c_{13} to be affected by plasticity.

Throughout the full pressure range from 16 to 66 GPa, our values for c_{11} and c_{13} continue to agree well with theoretical predictions, but c_{33} and c_{44} diverge rapidly from theory as plasticity progresses. c_{33} decreases until it becomes similar to c_{11} at ~ 30 GPa, and c_{44} increases rapidly and remains ~ 200 GPa higher than predicted. Plasticity strongly affects these two stiffnesses. Significant discrepancies between experimental and theoretical c_{33} and c_{44} even below 30 GPa,

which based on the differential stress analysis above is interpreted to be within the elastic regime, indicate that some plasticity modifies strain behavior even below widespread yielding.

3.3 Plastic Deformation

Plasticity may be evaluated based on the texture (non-random orientation distribution of crystallites) of the sample and lattice strains of a series of planes as observed as systematic azimuthal variations in diffraction intensity and d-spacing variation with azimuth (Fig. 5). The E-WIMV model implemented in MAUD software fits intensity variation (texture) in the Debye-Scherrer rings by generating an orientation distribution function that describes the frequency of crystallite orientations within the sample coordinate system [68]. The “Radial Diffraction in the DAC” stress model in the MAUD software fits the d-spacing variation with azimuth to obtain lattice strains. Deformation mechanisms can be investigated using EVPSC simulations, which model lattice strains and texture as a function of slip system activities and strength.

3.3.1 Texture Analysis

To determine crystallite orientation in bulk WC, the E-WIMV texture model was applied to each phase at each pressure step. Upon compression of WC up to 16 GPa, texture remained random. At 16 GPa, weak texture develops (figs. 5 and 10). Texture strength scaled in multiples of random distribution (m.r.d.) is observed to increase with pressure, particularly above 30 GPa, the pressure at which yielding was inferred from lattice strain. The development of texture supports the onset of plasticity at ~30 GPa (Fig. 11).

At the maximum pressure examined in this study, 66 GPa, the texture maximum in the inverse pole figure of the compression direction is near the $2\bar{1}\bar{1}0$ pole, which is the pole to the (100) in 3-coordinate *hkl* notation (Fig. 11). In the case of WC, (001) is the lattice plane supporting the highest strain and exhibiting the highest strength. Note that WC is a layered structure, with layers of C-atoms (graphene) orthogonal to 001, between hexagonal W layers [37]. The covalent C-C bonds within the layer are very strong, making deformation in the $\langle 001 \rangle$ direction extremely difficult. To determine which deformation mechanism(s) is consistent with generating this

preferred orientation in WC, modeling elasto-viscoplastic response of a polycrystalline WC aggregate is necessary.

3.3.2 Plasticity Simulation

Plasticity was simulated with an elasto-viscoplastic self-consistent (EVSPC) [69] model, modified for application to high-pressure experiments [70]. The model simultaneously reproduces refined Q values (lattice strain) and texture development at each pressure step and accounts for both elastic and viscoplastic deformation (Fig. 9). For our models we used theoretical elastic properties for WC [35]. The EVSPC model treats individual grains in a polycrystalline material as inclusions in an anisotropic homogeneous effective medium (HEM). The average of contributions from all grain inclusions determines the properties of the HEM matrix. Plasticity of a grain in the HEM matrix is then described by rate-sensitive constitutive equation for multiple slip systems:

$$\dot{\epsilon}_{ij} = \dot{\gamma}_0 \sum_s m_{ij}^s \left\{ \frac{|m_{kl}^s \sigma_{kl}|}{\tau^s} \right\}^n \text{sgn}(m_{kl}^s \sigma_{kl}), \quad (9)$$

where $\dot{\epsilon}_{ij}$ is the plastic strain rate, $\dot{\gamma}_0$ is the reference shear strain rate and τ^s is the critical resolved shear stress (CRSS) of the slip system s at the reference strain rate under conditions in the HEM. The grains are subject to local stress tensor σ_{kl} , the symmetric Schmid factor m_{kl}^s describes the straining direction of slip system s . When the stress resolved onto a given slip system is close to or above the threshold value, plastic deformation will occur on that slip system. The empirical stress exponent n describes strain rate sensitivity to applied stress, where infinite n implies rate-insensitivity. Deformation of WC appears to be rate insensitive [71] and consequently we assume an arbitrary high stress exponent of $n = 30$ [70], which is large enough to simulate rate insensitivity, yet small enough to preserve stability of the model.

The parameter τ^s represents the effective polycrystal CRSS and includes both strain hardening and pressure hardening. Pressure hardening and strain hardening effects on CRSS cannot be separated because both pressure and strain increase simultaneously in DAC experiments. Both are included in the pressure dependence of CRSS calculated by:

$$\tau^s = \tau_0^s + \frac{\partial \tau^s}{\partial P} P, \quad (10)$$

where τ_0^s is the initial CRSS value, and $\frac{\partial \tau^s}{\partial P}$ is its pressure-dependence. Values of CRSS and its pressure dependence for WC are presented in Table 3. The CRSS effectively controls slip system activity and different active slip systems [72] result in different lattice strains and texture and must be matched to experimental observations.

Lattice strain and texture evolution in WC are modeled simultaneously to determine deformation mechanisms such as slip system activity and slip system strength and is used to calculate yield stress from reproduced Q-values and texture (Fig. 7 and 11). Slip is activated at ~30 GPa on the $\{10\bar{1}0\}\langle\bar{1}2\bar{1}0\rangle$ prismatic slip system. From 30-40 GPa, this system converges towards ~50% of the slip system activity with the other 50% supported by $\{10\bar{1}0\}\langle 0001\rangle$ prismatic slip. Above 50 GPa, these systems each account for ~45% of the slip system activity, with the remaining 10% contributed from $\{10\bar{1}1\}\langle\bar{2}113\rangle$ pyramidal system (Fig. 12), which activates at ~40 GPa, and increases to 10% activity by 50 GPa. This slip system is needed to induce yielding on Q(001) and occurs in $\{10\bar{1}1\}$ rather than in $\{10\bar{1}0\}$ as described in previous work [39,40].

3.3.3 Crystallite Size and Microstrain

Refined values of grain size and microstrain in radial XRD patterns of bulk WC support the observed texture and modeled deformation mechanisms (Fig. 13). Mean anisotropic grain size decreases rapidly until plastic yielding, after which the grain size decreases slowly. Anisotropic crystallite size represents the size of coherently diffracting regions within the sample [73].

Local stresses can reduce the refined grain size by reducing the size of these regions, which can explain grain size reduction below plastic yielding [e.g. 74]. Microstrain increases with pressure until yielding, where it drops sharply and then begins to increase again. A second drop in microstrain may follow activation of slip on $\{10\bar{1}1\}\langle\bar{2}113\rangle$. Both microstrain and elastic macrostrain behavior as a function of pressure support elastic stress release in WC through plastic slip.

To further assess size and strain effects, we calculated size and strain contributions to peak broadening obtained from fitting individual peaks [after 75]. Size and microstrain affect peak widths with different dependencies on the Bragg angle θ . Assuming the size and strain components of peak broadening can be simply summed, the full width at half maximum of each peak β_{tot} is given by:

$$\beta_{tot} = \underline{C}\epsilon \tan \theta + \frac{K\lambda}{L \cos \theta}, \quad (11)$$

Multiplying both sides of this equation by $\cos \theta$ yields a line $\beta_{tot} \cos \theta$ vs. $\sin \theta$, where the slope $\underline{C}\epsilon$ is the strain component, and intercept $K\lambda/L$ is the size component. Peak widths and positions for planes 001, 100, and 101 were used for all analyses.

Size and strain as a function of pressure for bulk and nano-WC in Ne, and bulk WC with no medium are given in Fig. 14. Size contribution in the nano and bulk samples remains ~constant throughout the studied pressure range, consistent with no grain size reduction under the low shear stress supported by the Ne medium. The size effect in nano-WC is similar, but slightly larger than in bulk WC. Because the Ne medium is only quasi-hydrostatic, the strain contribution $\underline{C}\epsilon$ for both grain sizes compressed in Ne is similar and increases with increasing pressure and strength of the medium, but is less than the strain component observed in the sample without a medium. At pressures below 30 GPa in the bulk sample with no pressure medium, the size contribution increases due to convolution of lattice bending and some reduction in grain size. At 30 GPa in this nonhydrostatic sample, widespread yielding is indicated by a significant increase in size contribution $K\lambda/L$ and decrease in strain contribution $\underline{C}\epsilon$. Above 30 GPa, strain in nano-WC in Ne is intermediate between strain observed in bulk WC with and without the Ne medium. This is possibly due to the larger grain boundary surface area in nano-grain material being subjected to higher strain. Nano-crystalline WC may also be more sensitive to the increasing non-hydrostatic stress conditions exerted by the Ne pressure medium.

4. Discussion

4.1 Equation of State

Observed volumes for bulk WC obtained in this study under quasi-hydrostatic conditions are similar to data obtained in multi-anvil experiments on annealed WC, but systematically lower than volumes observed in previous DAC studies [1,2] (Fig. 2). Previous DAC studies employed less hydrostatic pressure-transmitting media: NaCl, methanol-ethanol solutions, and/or silicone oil are known to sustain significantly non-hydrostatic stress particularly at pressures above ~ 10 GPa [76–78]. Under nonhydrostatic axial compression, diffraction in axial geometry samples the crystallites near the orientation of minimum compression, and so obtains systematically larger calculated volumes and a correspondingly higher apparent incompressibility. The neon medium used in this study supports $< \sim 1$ GPa differential stress through the 64 GPa maximum pressure investigated here [e.g. 79], resulting in reliable quasi-hydrostatic volumes for constraining the EOS of WC.

Although previous work had suggested nano-WC is highly incompressible [2], data obtained under quasi-hydrostatic compression in this study demonstrate that nano-WC is not more incompressible than bulk WC. Observed volumes for bulk and nano-crystalline samples are indistinguishable at ambient conditions and remain similar upon compression. With increasing pressure, volumes obtained for nano-WC diverge to slightly smaller volumes relative to those for bulk WC. Previous work on nano-WC used silicone oil pressure medium [2], and as for bulk WC, may have overestimated incompressibility due to effects of non-hydrostatic stress. Based on our results for both bulk- and nano-WC compressed in Ne medium, we conclude there is no significant stiffening due to grain size; if anything, nano-WC is slightly less incompressible than bulk WC. This decrease in incompressibility with decreasing grain size in the nano-regime is consistent with observations for other ceramics cBN, TiO₂ and Al₂O₃ [23–25].

Understanding the effects of grain size on incompressibility is important for assessing overall elasto-viscoplastic responses of polycrystalline materials. Our bulk modulus value of 397 ± 7 GPa is in agreement with both theory and other hydrostatic experimental studies on WC. For

nanocrystalline WC, our bulk modulus value of 377 ± 7 is lower than the bulk value, and substantially lower than previous values reported for nano WC. A growing body of evidence indicates that while nano-scale grain size increases strength (e.g. the Hall-Petch effect), it decreases incompressibility for multiple incompressible materials, now including tungsten carbide. WC is among the least compressible materials, with incompressibility on par with cBN and cRuO₂ [cf. 14], but neither the bulk nor the nano-crystalline phase is as incompressible as diamond or higher- K_0 osmium borides[5,14].

4.2 Strength, Elasticity, and Deformation

The strength of bulk WC determined from lattice strain is comparable to other hard ceramics below 30 GPa pressure and 12-15 GPa differential stress is supported at the yield point of 30 GPa. The strength of WC determined by lattice strain is similar to that of TiB₂ and B₆O [80,81] (Fig. 10). It supports less differential stress than doped diamond [82], but is stronger than tungsten boride [83]. Reuss stresses provide information on strength anisotropy in WC, with (001) supporting the highest strength. Oriented WC crystals may provide a means of producing stronger parts without the need for binders. Lattice strain assumes purely elastic deformation however, and the determination of strength based on EVPSC modeling suggests a lower overall yield strength and flow stress when plasticity is considered. Plasticity affects the experimental results, and as noted by previous studies on other materials [84,85] strength from inferred elasticity may be overestimated in previous studies when not accounting for plasticity.

Deformation of WC above the yield stress includes both plastic and elastic components. The elastic stiffness coefficients calculated from our results only agree in part with theoretical calculations. This is consistent with observations of other materials in which plasticity is expected to occur. Previous experimental studies of elasticity based on radial diffraction have similarly observed that only some elastic constants agree with density functional theory predictions, while others diverge [e.g. 60,86]. This is attributed to the effects of plasticity [84,87]. In the case of rhenium[60], c_{11} and c_{12} , which describe stress and strain in the basal planes of the hexagonal

system, agree well with computations. In hcp cobalt [86,88], only c_{12} and c_{13} are in modest agreement with theory. In WC, c_{11} and c_{13} , representing stress and strain in both the basal and meridional planes, agree with theory but c_{12} , c_{33} , and c_{44} do not. Q-values are a function of both plasticity and elasticity and more work is needed to successfully solve for elastic stiffnesses in X-ray diffraction experiments on materials undergoing plastic deformation. Experimental values for the bulk and shear moduli at pressures > 15 GPa are needed to minimize error in calculations of c_{ij} s measured in X-ray diffraction experiments and provide additional constraints for theoretical predictions of these parameters. New theoretical computations accounting for experimental measurements of c/a with pressure is necessary to better constrain the pressure-dependence of the c_{ij} s, and to assess the effect of non-hydrostatic stress on hexagonal materials like Re and WC.

5. Conclusion

Our results demonstrate the mechanical response of WC under quasi-hydrostatic and non-hydrostatic compressive loads up to 66 GPa. As determined by our data and modeling, the strength of the (001) plane in WC is ~ 29 - 42% larger than the mean strength of WC. Plastic deformation in WC above yielding at 30 GPa is accommodated by prismatic slip on $\{10\bar{1}0\}\langle\bar{1}2\bar{1}0\rangle$ and $\{10\bar{1}0\}\langle 0001\rangle$, and pyramidal slip on $\{10\bar{1}1\}\langle\bar{2}113\rangle$. WC anvils should be oriented to the strongest direction to maximize strength performance under pressure. The new constraints provided by this study on the strength, deformation, and EOS of WC can help inform production of WC parts, and potentially applications of polycrystalline materials more broadly, for research and industry.

Declaration of Competing Interest

The authors declare that they have no known competing financial interests or personal relationships that could have appeared to influence the work reported in this paper.

Acknowledgements

The authors would like to acknowledge Garrett Diedrich, Wanyue Peng, and Gill Levental for their support and assistance during data collection.

Funding Sources

This work was supported by the U.S. Department of Energy — National Nuclear Security Administration (Capital-DOE Alliance Center DE-NA0003858) and National Science Foundation (EAR 1663442 and EAR 1654687). This work was performed at HPCAT (Sector 16), Advanced Photon Source (APS), Argonne National Laboratory. HPCAT operations are supported by DOE-NNSA's Office of Experimental Sciences. The Advanced Photon Source is a U.S. Department of Energy (DOE) Office of Science User Facility operated for the DOE Office of Science by Argonne National Laboratory under Contract No. DE-AC02-06CH11357. Use of the Advanced Photon Source was supported by the U. S. Department of Energy, Office of Science, Office of Basic Energy Sciences, under Contract No. DE-AC02-06CH11357.

Tables and Figures
Table 1: Experimental and theoretical values for the equation of state parameters for hexagonal tungsten monocarbide. US = ultrasonic, SW = shock wave, DAC = diamond anvil cell, MAP = multi-anvil press, XRD = X-ray diffraction, LDA = local-density approximation, GGA = generalized gradient approximation, PWP = plane wave potential, PBE = Perdew, Burke, and Ernzerhof, LMTO = linear muffin-tin orbital. Values and uncertainties reported for this work are obtained from fit to the Birch-Murnaghan equation of state.

$V_0(\text{\AA}^3)$	$K_0(\text{GPa})$	K_0'	Grain Size	Method	Reference
20.4667	329	-	not specified	US	[22]
20.707-20.747	383	-	not specified	SW	[59]
-	390.3	-	not specified	US	[7]
20.806 ± 0.020	383.8 ± 0.8	2.61 ± 0.07	Bulk	US	[1]
20.806 ± 0.020	411.8 ± 12.1	5.45 ± 0.73	Bulk	DAC XRD, NaCl, silicone oil, and 4:1 methanol-ethanol solution	[1]
20.749	452.2 ± 7.8	1.25 ± 0.53	Nano	DAC XRD, silicone oil	[2]
20.750 ± 0.002	384 ± 4	4.65 ± 0.32	Bulk	MAP XRD, MgO	[10]
20.75 ± 0.00	387 ± 5	4.38 ± 0.40	Bulk	MAP XRD, MgO	BM-EOS fit to [10]
20.76 ± 0.01	397 ± 7	3.7 ± 0.3	Bulk	DAC XRD, Ne	This study
20.74 (fixed)	412 ± 4	3.3 ± 0.2	Bulk	DAC XRD, Ne	This study
20.74 ± 0.01	377 ± 7	3.8 ± 0.3	Nano	DAC XRD, Ne	This study
20.72 (fixed)	388 ± 5	3.5 ± 0.2	Nano	DAC XRD, Ne	This study
$V_0(\text{\AA}^3)$	$K_0(\text{GPa})$	K_0'	Exchange-correlation functional		Reference
-	655	-	not specified		[89]
-	404	-	GGA		[90]
20.5267	382.4	-	GGA		[32]
-	382.4	-	GGA		[33]
-	392.5	-	LDA		[34]
20.749	390.2 ± 0.5	4.19 ± 0.04	LDA		[2]
20.6558	393	-	GGA		[8]
20.6558	400.9	4.06	GGA		[8]
21.240	356	-	GGA		[91]
21.33	373	4.40	GGA		[21]
-	389.4	4.16	GGA		[35]
20.99	389.6	4.27	GGA		[36]

470

471

Table 2: Observed pressures and lattice parameters with uncertainties from UnitCell [56] fit of d -spacings for bulk and nano-crystalline WC.

Bulk			Nano		
Pressure (GPa)	Lattice parameter		Pressure (GPa)	Lattice parameter	
	a (Å)	c (Å)		a (Å)	c (Å)
1 Bar	2.9049 ± 0.0001	2.8378 ± 0.0004	1 Bar	2.905 ± 0.0002	2.838 ± 0.0004
0.9	2.9038 ± 0.0002	2.8370 ± 0.0004	0.9	2.902 ± 0.0002	2.838 ± 0.0004
3	2.8979 ± 0.0002	2.8324 ± 0.0004	1	2.899 ± 0.0002	2.837 ± 0.0004
6	2.8923 ± 0.0002	2.8277 ± 0.0004	4	2.894 ± 0.0002	2.832 ± 0.0004
8	2.8854 ± 0.0002	2.8220 ± 0.0004	7	2.886 ± 0.0002	2.823 ± 0.0004
10	2.8800 ± 0.0002	2.8180 ± 0.0004	13	2.871 ± 0.0002	2.812 ± 0.0004
13	2.8756 ± 0.0002	2.8142 ± 0.0004	18	2.860 ± 0.0001	2.803 ± 0.0004
15	2.8707 ± 0.0002	2.8111 ± 0.0004	23	2.848 ± 0.0001	2.792 ± 0.0003
18	2.8635 ± 0.0001	2.8045 ± 0.0004	28	2.838 ± 0.0001	2.784 ± 0.0003
21	2.8574 ± 0.0001	2.7993 ± 0.0004	32	2.828 ± 0.0001	2.777 ± 0.0003
24	2.8503 ± 0.0001	2.7940 ± 0.0004	35	2.822 ± 0.0001	2.772 ± 0.0003
27	2.8446 ± 0.0001	2.7891 ± 0.0003	39	2.815 ± 0.0001	2.768 ± 0.0001
30	2.8377 ± 0.0001	2.7831 ± 0.0003	46	2.803 ± 0.0001	2.758 ± 0.0003
34	2.8303 ± 0.0001	2.7779 ± 0.0003	49	2.796 ± 0.0001	2.752 ± 0.0003
39	2.8218 ± 0.0001	2.7710 ± 0.0003	53	2.792 ± 0.0001	2.745 ± 0.0003
42	2.8153 ± 0.0001	2.7646 ± 0.0003	56	2.785 ± 0.0001	2.741 ± 0.0003
46	2.8090 ± 0.0001	2.7607 ± 0.0003	60	2.778 ± 0.0001	2.736 ± 0.0003
47	2.8056 ± 0.0001	2.7562 ± 0.0003	64	2.770 ± 0.0001	2.733 ± 0.0003
51	2.7983 ± 0.0001	2.7508 ± 0.0003			
54	2.7944 ± 0.0001	2.7471 ± 0.0003			
55	2.7921 ± 0.0001	2.7453 ± 0.0003			
59	2.7879 ± 0.0001	2.7423 ± 0.0003			

477 **Table 3:** CRSS and pressure dependence values for active slip systems in WC under non-
478 hydrostatic compressive stress.

Slip System	Slip Mechanism	CRSS (GPa)	d(CRSS)/dP
$\{10\bar{1}0\}\langle\bar{1}2\bar{1}0\rangle$	Prismatic	4.0	0.065
$\{10\bar{1}0\}\langle 0001\rangle$	Prismatic	2.6	0.065
$\{10\bar{1}1\}\langle\bar{2}113\rangle$	Pyramidal	14.0	0.08

479

480

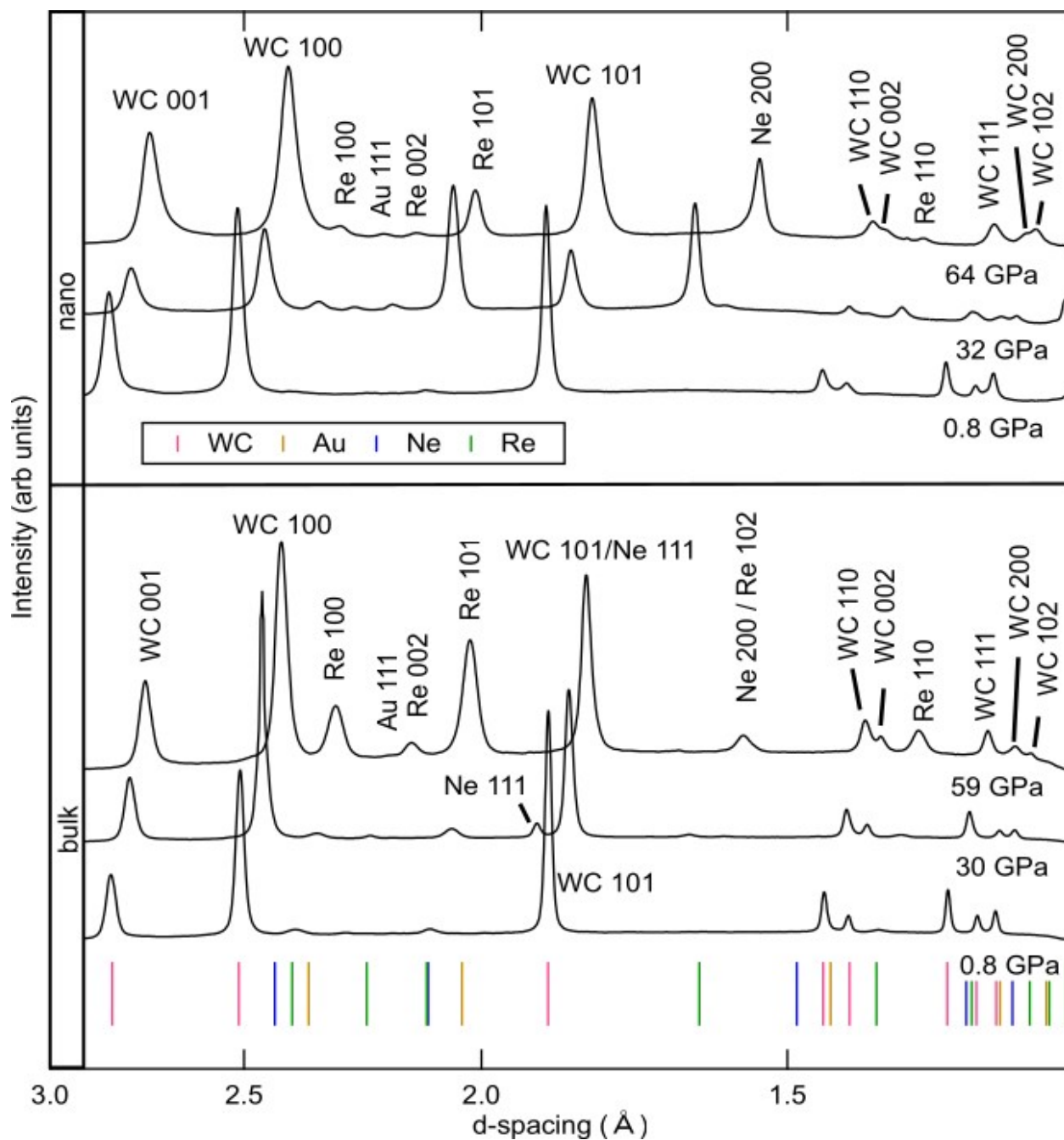


Figure 1. Representative synchrotron X-ray diffraction patterns of bulk and nano-crystalline WC compressed in Ne pressure medium with Au pressure standard and Re gasket in the axial diffraction geometry.

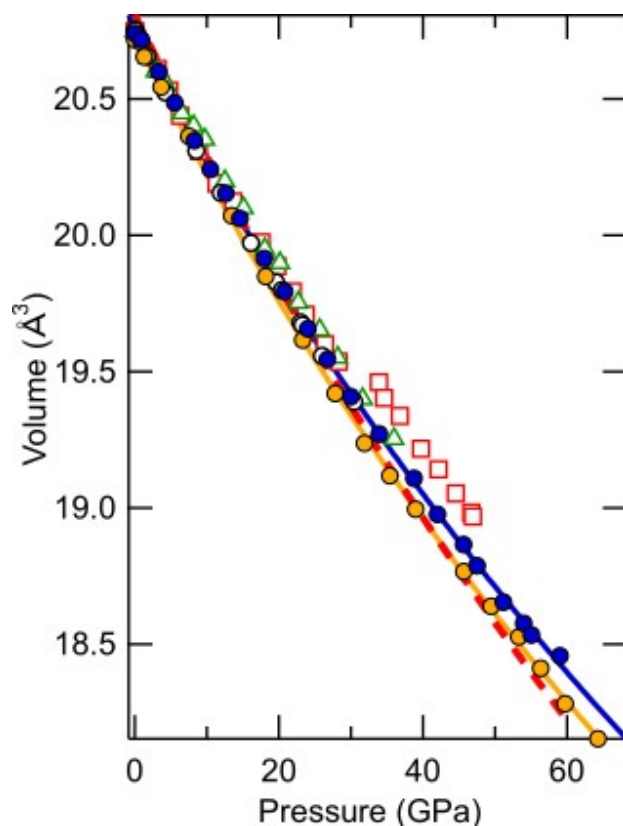


Figure 2: Compression of bulk (blue circles, with 3rd order Birch-Murnaghan equation of state fit in blue line) and nanocrystalline (yellow circles, with EoS fit in yellow line) WC in Ne compared with other experimental studies. Pressure was determined from the EOS of Au, using the 111, 200, and 220 Au peaks and the pressure scale of Dewaele [48]. Data from previous studies was obtained in the multi-anvil press [10] (black open circles) and in the DAC for bulk (red open squares [1]) and nano-crystalline WC (green open triangles [2]). Ultrasonic measurements [1] are displayed in red solid line and extrapolated with red dashed line.

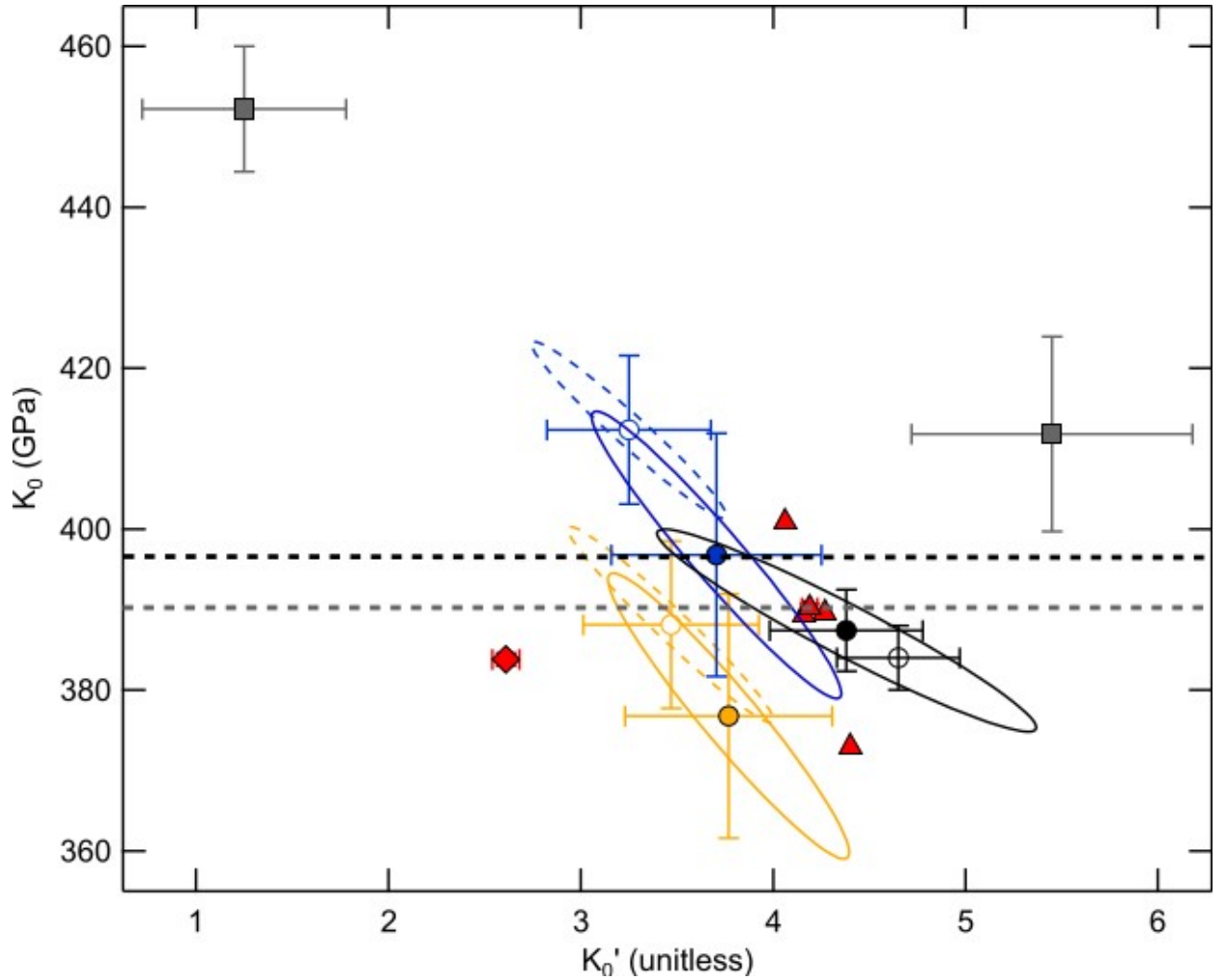


Figure 3: Ellipses representing 95.3% confidence in K_0 and K'_0 obtained from Birch-Murnaghan equation fit to pressure-volume data for bulk (blue, this study and black, room temperature data from multi-anvil [10]), and nano-grained WC (yellow). Dashed ellipses with open circles are with V_0 fixed to ambient XRD measurements, solid ellipses with solid circles are with V_0 fit. The open gray circle indicates reported values from multi-anvil, high-temperature/pressure EOS [10]. Solid gray squares are from other DAC studies on nano-crystalline [2] and bulk [1]. Red triangles indicate values obtained from theoretical calculations [2,8,21,35,36]. The solid red diamond is the adiabatic bulk modulus from ultrasonic experiments [1]. Dashed lines are from shock wave (black line [59]) and ultrasonic interferometry experiments (gray line [89]), which only constrain K_0 but not K'_0 .

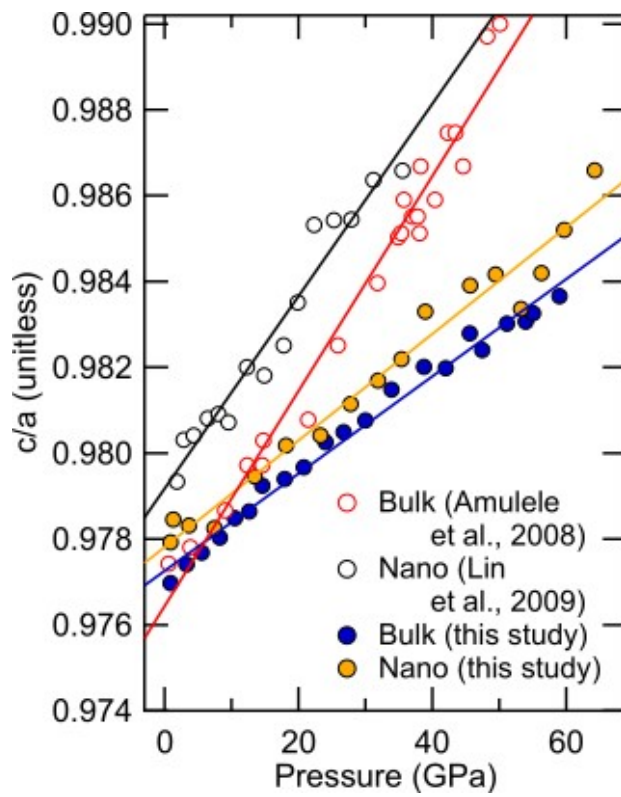


Figure 4 The ratio c/a vs P for bulk- and nano-grain WC from experimental measurements. Values obtained using nonhydrostatic media (open circles) are systematically higher than with hydrostatic media (filled circles, this study).

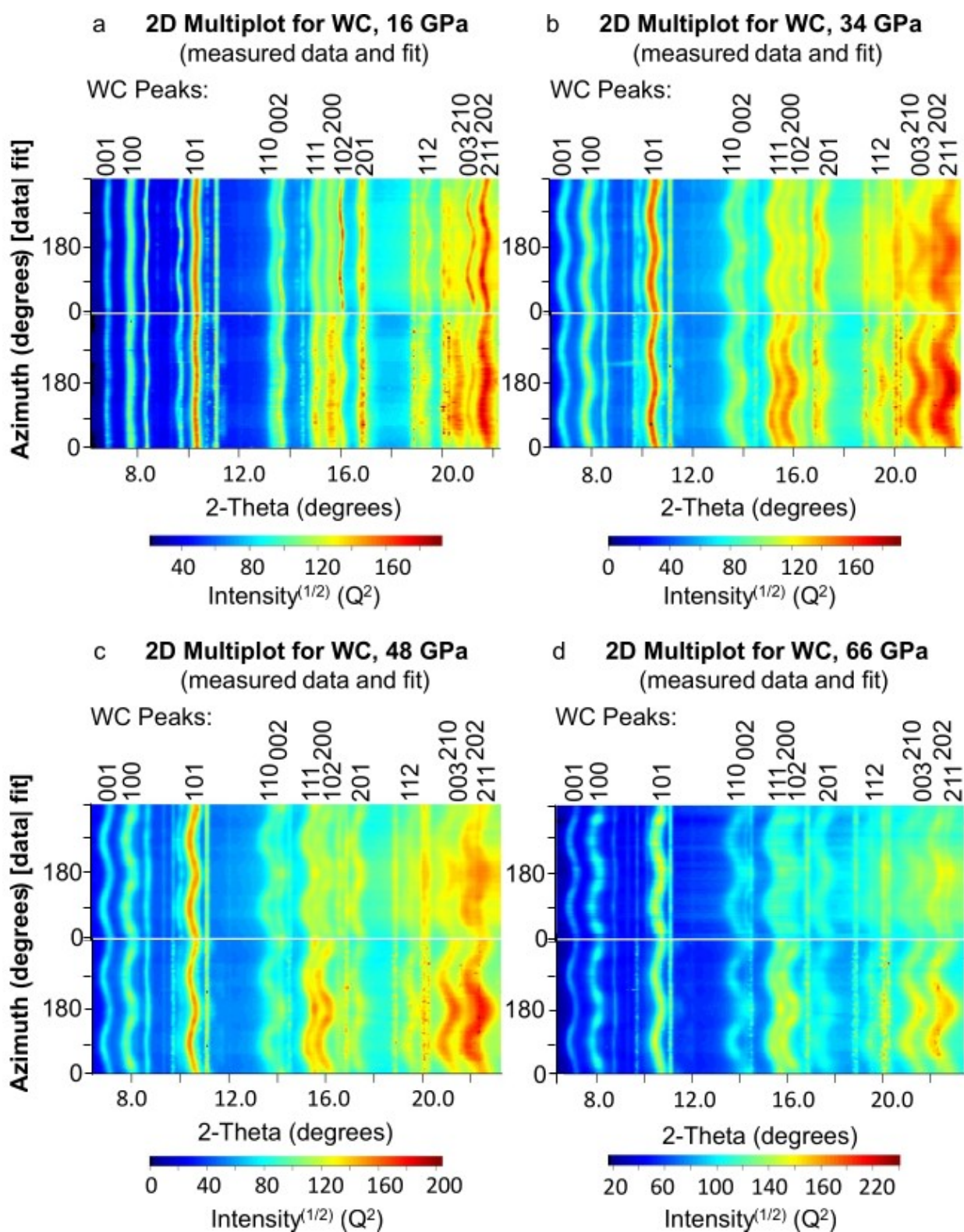


Figure 5: X-ray diffraction pattern data (lower half of each image) and full-profile refinements (upper half of each image) for selected pressures a) 16 GPa, b) 34 GPa, c) 48 GPa and d) 66 GPa. The Debye-Scherrer rings are transformed to azimuth vs 2 θ and Miller indices for WC are labeled in each pattern. WC peaks exhibit increasing sinusoidal curvature with pressure due to non-hydrostatic strain. Systematic

513 variation in intensity in individual diffraction lines is indicative of plastic deformation and also increases
514 with pressure in WC. Diffracting planes from gasket materials Be and BeO at ambient conditions are also
515 observed and exhibit no strain.

516

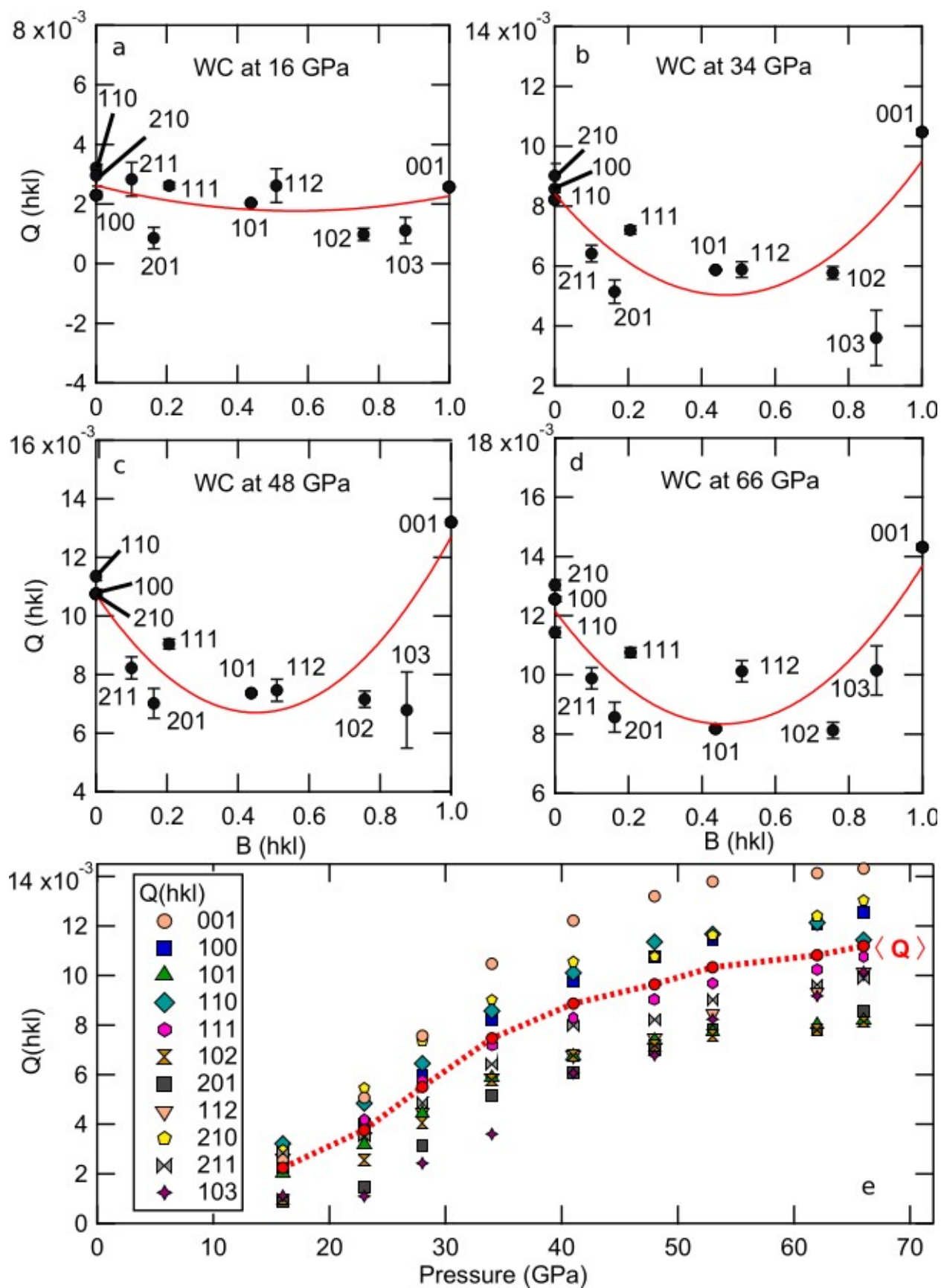


Figure 6: Strain obtained for WC lattice planes $Q(hkl)$ at selected pressures plotted vs. the orientation function $B(hkl)$ (eqn 4) relative to the stress axis (a-d) and for all planes as pressure increases (e). In (a-d), red curves are quadratic fits to strain $Q(hkl)$ vs. $B(hkl)$. Strain anisotropy increases with pressure (scaling is constant for Figures a-d). Error in $Q(hkl)$ at individual pressures represents the error of the refinement to the experimentally observed curvature. In e), the mean strain $\langle Q \rangle$ (red circles and dashed line between points for emphasis) increases monotonically, and the shape of the Q vs P curve is similar for all $Q(hkl)$, however values diverge in Q as pressure increases, indicating an increase in anisotropy as pressure increases.

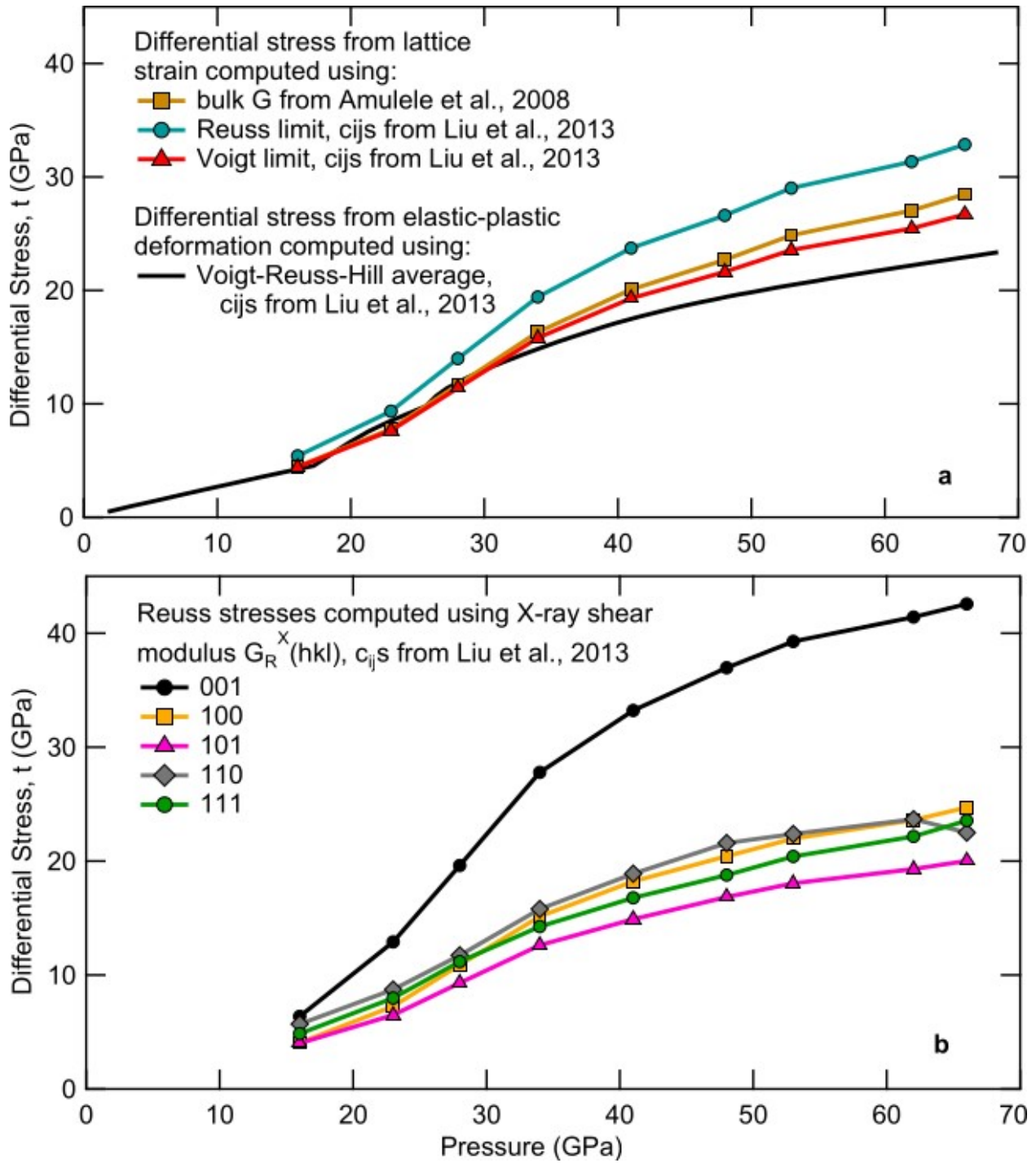
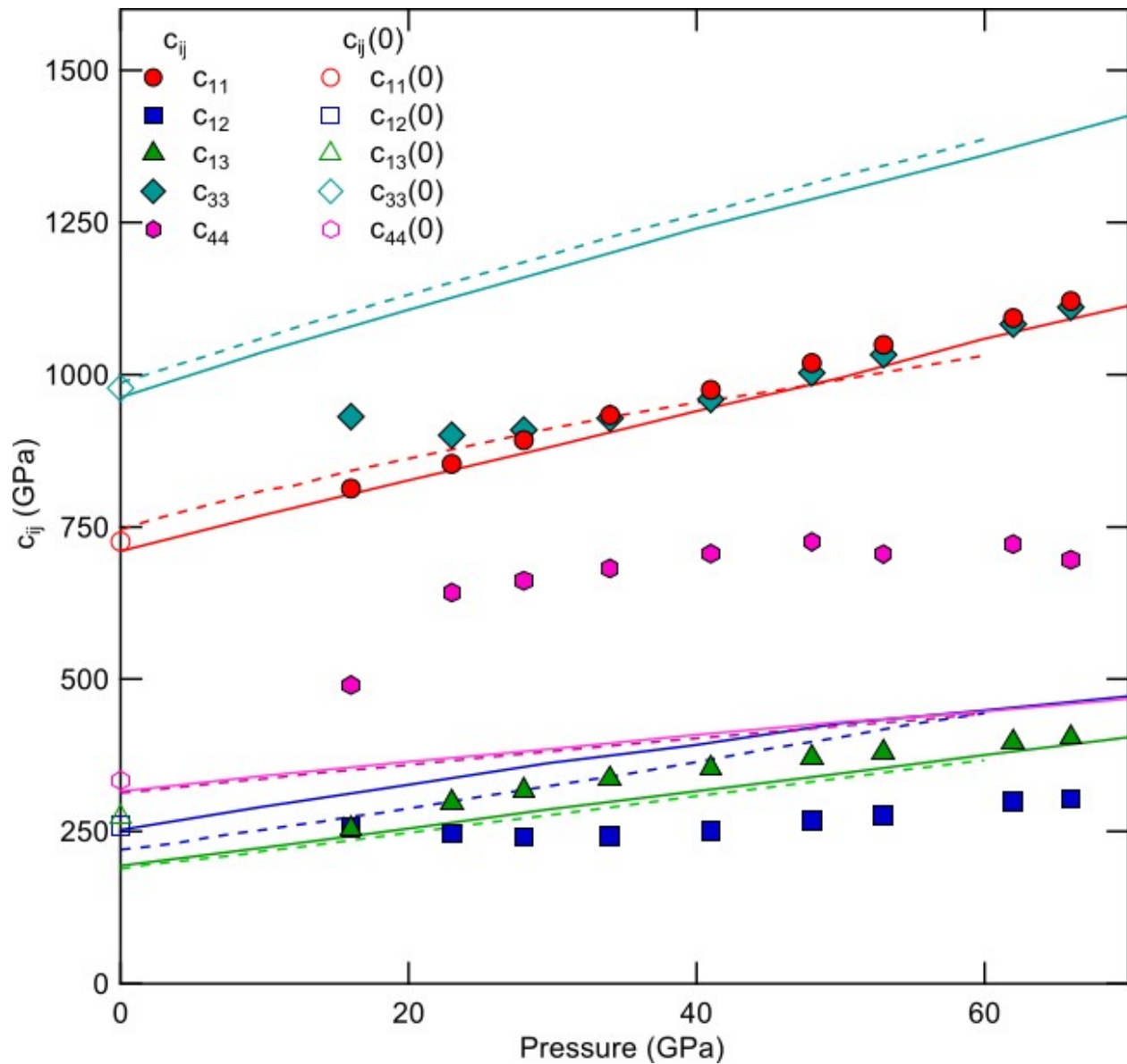


Figure 7: Differential stress t in WC obtained from lattice strain analysis and EVPSC model of experimental measurements. Figure 7a (left): Average Voigt (red triangles) and Reuss (teal circles) values for differential stress computed from $Q(hkl)$ and elastic constants obtained from theoretical calculations [35], with values obtained using aggregate shear modulus (gold squares [1]). Also shown is differential stress obtained from EVPSC simulation incorporating texture and plasticity (solid black line). Stress accounting only for elastic strain diverges from stress accounting for both elastic and plastic strain at the yield point near 30 GPa. Figure 7b (right): Reuss stresses computed for individual lattice planes hkl using

534 purely elastic strain. (001) supports the largest differential stress ~28 GPa, ~29-42% larger than
535 differential stress values of ~16-20 GPa at yielding, which use the aggregate and Reuss-limit shear
536 modulus, respectively, and 57% larger than the stress from the EVPSC model.

537



539

540 **Figure 7:** Elastic stiffness coefficients for experimental data as calculated from eqns (1-6, and 8) (closed
 541 symbols: this study). Open symbols are experimental zero-pressure values [31]. Solid and dashed lines are
 542 from theoretical calculations [35,36]. Our values for c_{11} and c_{13} agree well with theoretical predictions.
 543 Other c_{ij} s are closest to DFT values at minimum pressure (closest to pure elastic deformation), providing
 544 validation for DFT. Stiffnesses deviate from predicted values rapidly as plastic deformation increases,
 545 illustrating mechanisms of failure. Above yielding at 30 GPa, values for c_{44} is substantially higher than
 546 predicted, and c_{33} and c_{12} diverge from predicted values. Values for c_{33} appear to converge with c_{11} , while
 547 c_{12} varies only slightly from a constant value of 200 GPa throughout the experimental pressure interval.

548

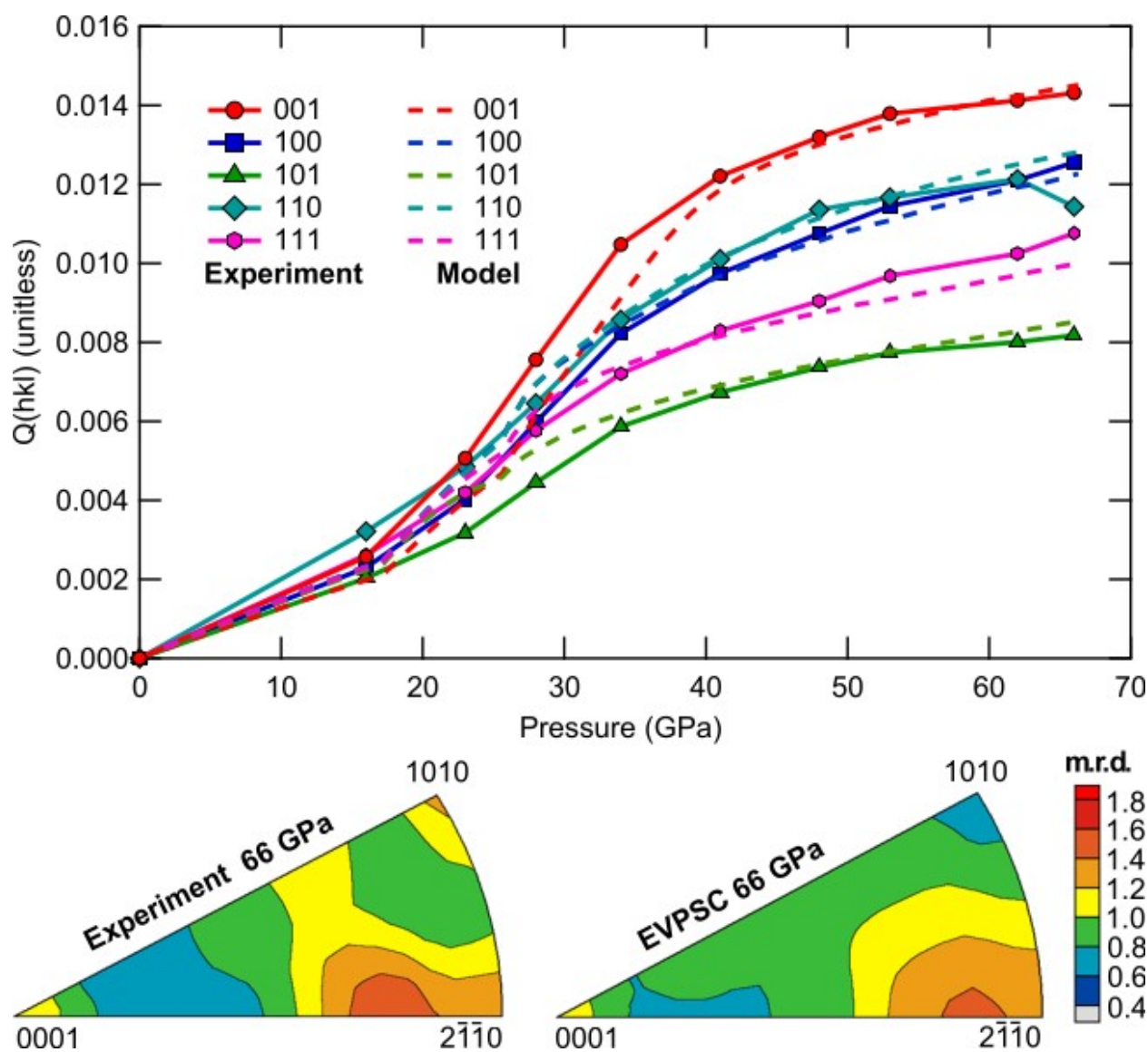


Figure 8 Strain and texture in WC. *Left:* Experimental and modeled strain (Q-factors) for selected planes of WC vs. pressure. *Right:* Experimental (top) and modeled (bottom) inverse pole figures illustrating non-random texture at 66 GPa.

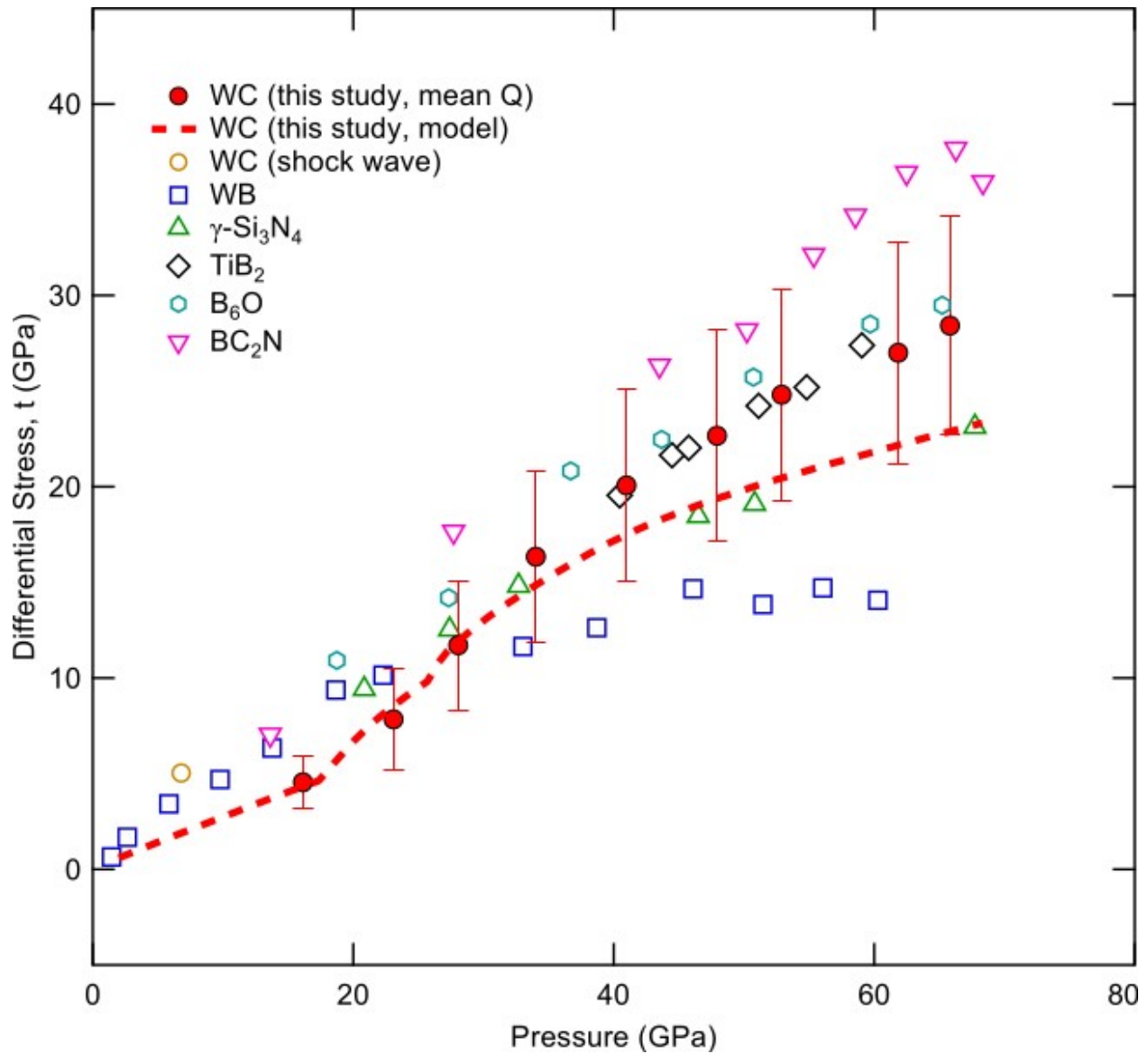


Figure 10: Differential stress observed in WC and other hard ceramics compressed uniaxially with no pressure-transmitting medium. Stress in WC is computed with both lattice strain theory (solid circles) and EVPSC simulation (dashed line). Dynamic yield strength from shock wave data is open gold circle, calculated after [92]. Previous studies on all other hard ceramics (open symbols) use lattice strain theory. Blue squares are WB [83], green triangles are γ -Si₃N₄ [93], black diamonds are TiB₂ [81], teal hexagons are B₆O [80], and magenta triangles are BC₂N heterodiamond [82]. Uncertainty is calculated as \pm the standard deviation in mean Q at each pressure, propagated through equation (6). Differential stress increases with uniaxial load until yielding, where the change in slope of the $t(P)$ indicates strain is accommodated by both elastic and plastic deformation. In WC, yielding at 30 GPa is supported by the development of texture at the same pressure (Fig. 11). The flow stress of WC above yielding is higher than flow stresses observed in WB and Si₃N₄. Flow stress obtained from EVPSC simulation is systematically lower than that derived from lattice strain analysis only, though the results of the two methods remain within uncertainty of each other.

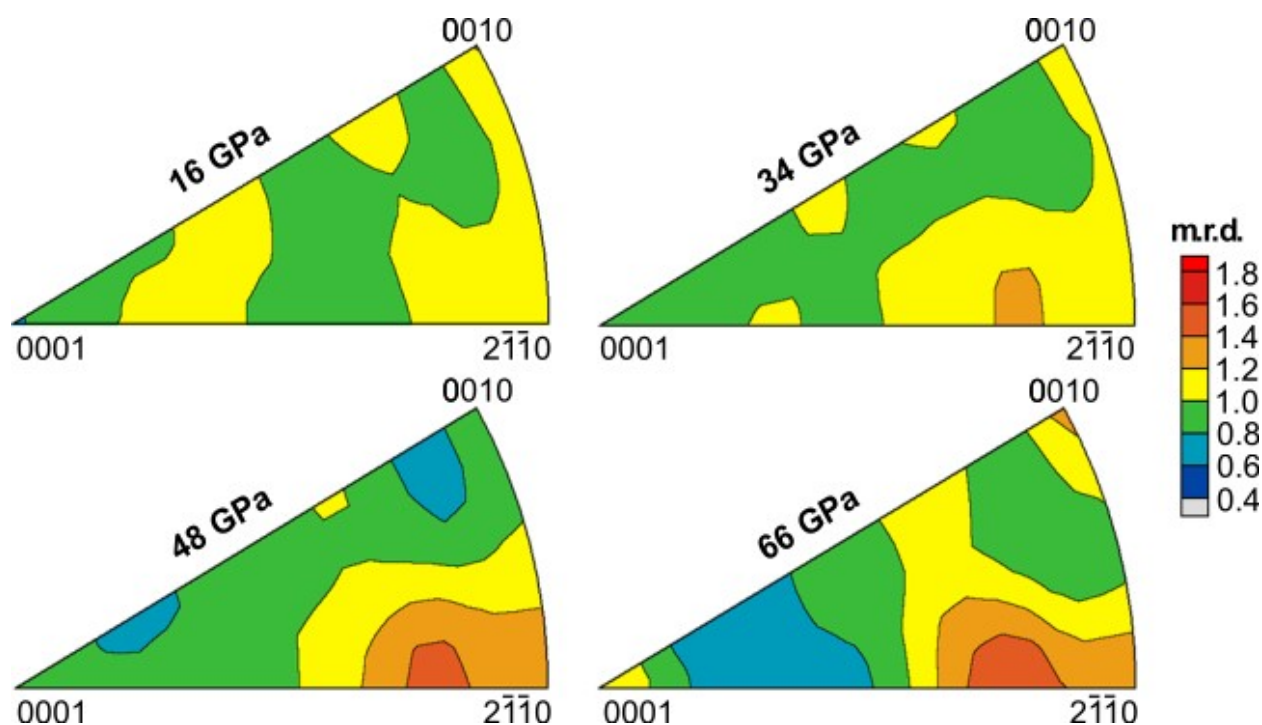


Figure 9: Inverse pole figures reconstructed from experimental ODF data fit with fiber texture at selected pressures. A texture maximum is observed at ~30 GPa near the 2-1-10 planes (symmetrically equivalent to 100 planes in hkl notation), indicating plastic deformation. This value increases to ~1.9 multiples of a random distribution at the maximum pressure of 66 GPa.

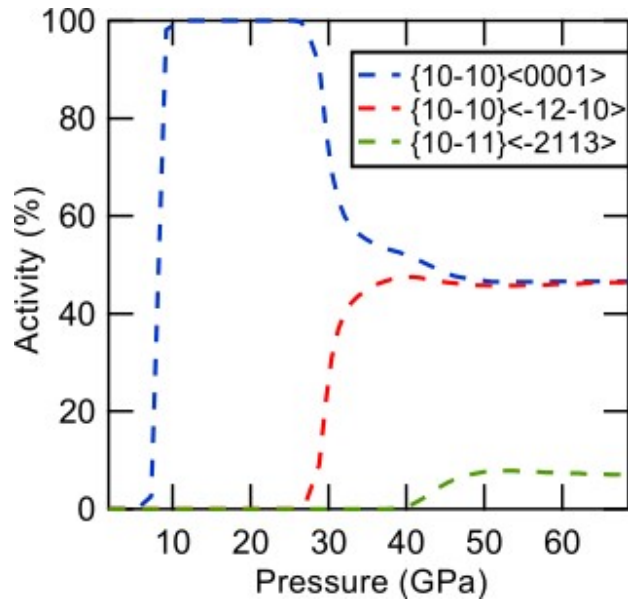


Figure 10: Modeled slip system activities as determined from the EVPSC simulation. Based on experimental texture, below 8 GPa, deformation is entirely elastic, and no plastic deformation occurs. Between 8-30 GPa, a small amount of plastic strain is accommodated by prismatic slip activation on $\{10\bar{1}0\}\langle 0001 \rangle$. At 30 GPa, bulk plastic yielding occurs, accommodated by continued prismatic slip on $\{10\bar{1}0\}\langle 0001 \rangle$ and activation of prismatic slip on $\{10\bar{1}0\}\langle \bar{1}2\bar{1}0 \rangle$. A third (pyramidal) slip system is activated between 40-50 GPa on $\{10\bar{1}1\}\langle \bar{2}113 \rangle$.

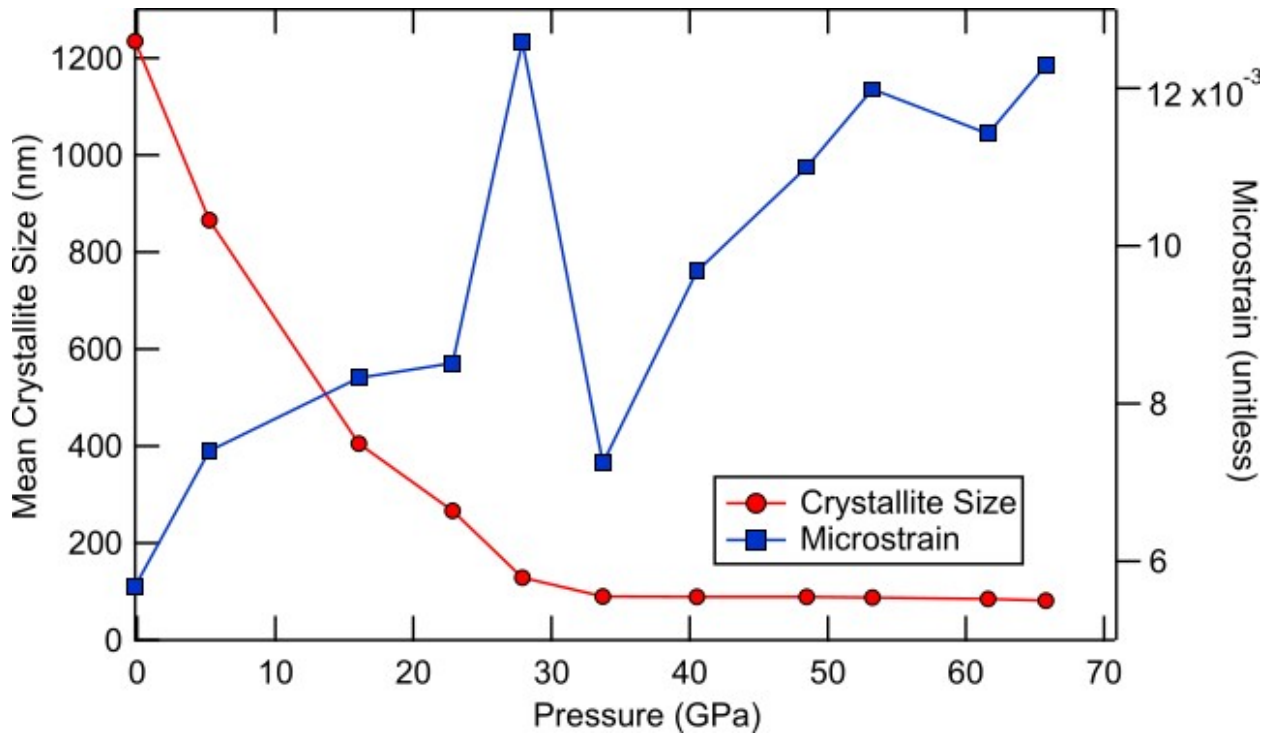
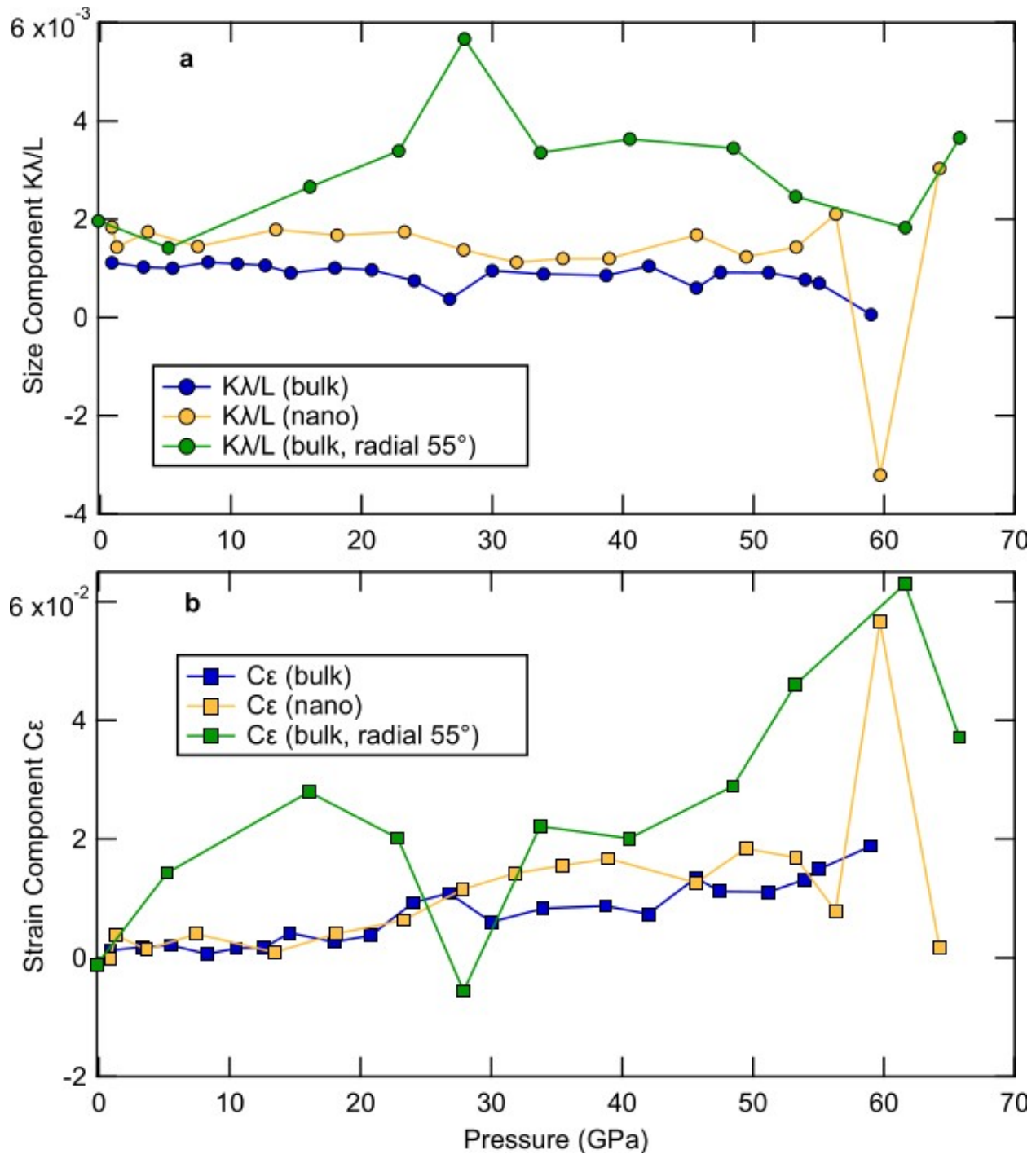


Figure 11: Crystallite size and microstrain vs pressure from full-profile refinement in WC under non-hydrostatic compression. Crystallite size decreases and microstrain increases up to ~30 GPa, the pressure at which lattice strain suggests yielding and texture indicates activation of prismatic slip on $\{10\bar{1}0\}\{\bar{1}2\bar{1}0\}$ and $\{10\bar{1}0\}\{0001\}$. Reduction in crystallite size below plasticity onset is attributed to lattice-bending, which reduces the size of the coherently diffracting regions contributing to crystallite size in MAUD software. Above 30 GPa, microstrain drops and then resumes increasing, while grain size remains ~constant at ~80 - 90 nm. A second dip in microstrain at ~50 GPa follows the activation of pyramidal slip on $\{10\bar{1}1\}\{\bar{2}113\}$.



594

595 **Figure 14:** Williamson-Hall [75] analysis of size (a) and strain (b) components of peak-width as a
 596 function of pressure for bulk (blue), nano (yellow), and bulk radial (green) WC. Size contributes more to
 597 peak-broadening in the bulk radial analysis than in the analysis of bulk or nano in the axial geometry. Size
 598 is expected to affect peak broadening in the radial geometry, because of the absence of a pressure medium
 599 induces plastic deformation. The largest size effect is observed at the yield point. The strain contribution
 600 is larger in the radial geometry below the yield point than for bulk or nano-grain WC. Strain increases
 601 smoothly and ~monotonically in the bulk in Ne and nano in Ne at low pressures, but just below 30 GPa

602 both the nano-crystalline WC in Ne and bulk WC with no medium exhibit a decrease in strain followed
603 by a sharp increase.

604

References

- [1] G.M. Amulele, M.H. Manghnani, S. Marriappan, X. Hong, F. Li, X. Qin, H.P. Liermann, Compression behavior of WC and WC-6%Co up to 50 GPa determined by synchrotron x-ray diffraction and ultrasonic techniques, *J. Appl. Phys.* 103 (2008) 113522. <https://doi.org/10.1063/1.2938024>.
- [2] Z. Lin, L. Wang, J. Zhang, H. Mao, Y. Zhao, Nanocrystalline tungsten carbide: As incompressible as diamond, *Appl. Phys. Lett.* 95 (2009) 211906. <https://doi.org/10.1063/1.3268457>.
- [3] V.T. Golovchan, On the strength of polycrystalline tungsten monocarbide, *Int. J. Refract. Met. Hard Mater.* 28 (2010) 250–253. <https://doi.org/10.1016/j.ijrmhm.2009.10.006>.
- [4] B. Roebuck, P. Klose, K.P. Mingard, Hardness of hexagonal tungsten carbide crystals as a function of orientation, *Acta Mater.* 60 (2012) 6131–6143. <https://doi.org/10.1016/j.actamat.2012.07.056>.
- [5] M.T. Yeung, R. Mohammadi, R.B. Kaner, Ultraincompressible, Superhard Materials, *Annu. Rev. Mater. Res.* 46 (2016) 465–485. <https://doi.org/10.1146/annurev-matsci-070115-032148>.
- [6] M.W. Cook, P.K. Bossom, Trends and recent developments in the material manufacture and cutting tool application of polycrystalline diamond and polycrystalline cubic boron nitride, *Int. J. Refract. Met. Hard Mater.* 18 (2000) 147–152. [https://doi.org/10.1016/S0263-4368\(00\)00015-9](https://doi.org/10.1016/S0263-4368(00)00015-9).
- [7] M. Lee, R.S. Gilmore, Single crystal elastic constants of tungsten monocarbide, *J. Mater. Sci.* 17 (1982) 2657–2660. <https://doi.org/10.1007/BF00543901>.
- [8] Y. Li, Y. Gao, B. Xiao, T. Min, Z. Fan, S. Ma, L. Xu, Theoretical study on the stability, elasticity, hardness and electronic structures of W–C binary compounds, *J. Alloys Compd.* 502 (2010) 28–37. <https://doi.org/10.1016/j.jallcom.2010.04.184>.
- [9] M.L. Benea, L.P. Benea, Characterization of the WC coatings deposited by plasma spraying, *IOP Conf. Ser. Mater. Sci. Eng.* 85 (2015) 012004. <https://doi.org/10.1088/1757-899X/85/1/012004>.
- [10] K.D. Litasov, A. Shatskiy, Y. Fei, A. Suzuki, E. Ohtani, K. Funakoshi, Pressure-volume-temperature equation of state of tungsten carbide to 32 GPa and 1673 K, *J. Appl. Phys.* 108 (2010) 053513. <https://doi.org/10.1063/1.3481667>.
- [11] T. Ishii, D. Yamazaki, N. Tsujino, F. Xu, Z. Liu, T. Kawazoe, T. Yamamoto, D. Druzhbin, L. Wang, Y. Higo, Y. Tange, T. Yoshino, T. Katsura, Pressure generation to 65 GPa in a Kawai-type multi-anvil apparatus with tungsten carbide anvils, *High Press. Res.* 37 (2017) 507–515. <https://doi.org/10.1080/08957959.2017.1375491>.
- [12] L. Silvestroni, N. Gilli, A. Migliori, D. Sciti, J. Watts, G.E. Hilmas, W.G. Fahrenholtz, Binderless WC with high strength and toughness up to 1500 °C, *J. Eur. Ceram. Soc.* 40 (2020) 2287–2294. <https://doi.org/10.1016/j.jeurceramsoc.2020.01.055>.
- [13] D. Yamazaki, E. Ito, T. Yoshino, N. Tsujino, A. Yoneda, H. Gomi, J. Vazhakuttiyakam, M. Sakurai, Y. Zhang, Y. Higo, Y. Tange, High-pressure generation in the Kawai-type multi-anvil apparatus equipped with tungsten-carbide anvils and sintered-diamond anvils, and X-ray observation on CaSnO₃ and (Mg,Fe)SiO₃, *Comptes Rendus Geosci.* 351 (2019) 253–259. <https://doi.org/10.1016/j.crte.2018.07.004>.
- [14] J. Haines, J. Léger, G. Bocquillon, Synthesis and Design of Superhard Materials, *Annu. Rev. Mater. Res.* 31 (2001) 1–23. <https://doi.org/10.1146/annurev.matsci.31.1.1>.
- [15] J.J. Gilman, R.W. Cumberland, R.B. Kaner, Design of hard crystals, *Int. J. Refract. Met. Hard Mater.* 24 (2006) 1–5. <https://doi.org/10.1016/j.ijrmhm.2005.05.015>.
- [16] Q. Gu, G. Krauss, W. Steurer, Transition Metal Borides: Superhard versus Ultra-incompressible, *Adv. Mater.* 20 (2008) 3620–3626. <https://doi.org/10.1002/adma.200703025>.
- [17] Z.Z. Fang, X. Wang, T. Ryu, K.S. Hwang, H.Y. Sohn, Synthesis, sintering, and mechanical properties of nanocrystalline cemented tungsten carbide – A review, *Int. J. Refract. Met. Hard Mater.* 27 (2009) 288–299. <https://doi.org/10.1016/j.ijrmhm.2008.07.011>.

- [18] I.P. Borovinskaya, V.I. Vershinnikov, T.I. Ignatieva, Tungsten Carbide, in: Concise Encycl. Self-Propagating High-Temp. Synth., Elsevier, 2017: pp. 406–407. <https://doi.org/10.1016/B978-0-12-804173-4.00162-9>.
- [19] W.R. Taylor, S.F. Foley, Improved oxygen-buffering techniques for C-O-H fluid-saturated experiments at high pressure, *J. Geophys. Res. Solid Earth*. 94 (1989) 4146–4158. <https://doi.org/10.1029/JB094iB04p04146>.
- [20] Q. Fang, W. Bai, J. Yang, X. Xu, G. Li, N. Shi, M. Xiong, H. Rong, Qusongite (WC): A new mineral, *Am. Mineral*. 94 (2009) 387–390. <https://doi.org/10.2138/am.2009.3015>.
- [21] X.Y. Cheng, J.H. Zhou, X. Xiong, Y. Du, C. Jiang, First-principles thermal equation of state of tungsten carbide, *Comput. Mater. Sci*. 59 (2012) 41–47. <https://doi.org/10.1016/j.commatsci.2012.02.028>.
- [22] H.L. Brown, P.E. Armstrong, C.P. Kempter, Elastic Properties of Some Polycrystalline Transition-Metal Monocarbides, *J. Chem. Phys*. 45 (1966) 547–549. <https://doi.org/10.1063/1.1727602>.
- [23] Y. Le Godec, O.O. Kurakevych, P. Munsch, G. Garbarino, M. Mezouar, V.L. Solozhenko, Effect of nanostructuration on compressibility of cubic BN, *J. Superhard Mater*. 34 (2012) 336–338. <https://doi.org/10.3103/S1063457612050085>.
- [24] B. Chen, D. Penwell, L.R. Benedetti, R. Jeanloz, M.B. Kruger, Particle-size effect on the compressibility of nanocrystalline alumina, *Phys. Rev. B*. 66 (2002) 144101. <https://doi.org/10.1103/PhysRevB.66.144101>.
- [25] Y. Al-Khatatbeh, K.K.M. Lee, B. Kiefer, Compressibility of Nanocrystalline TiO₂ Anatase, *J. Phys. Chem. C*. 116 (2012) 21635–21639. <https://doi.org/10.1021/jp3075699>.
- [26] X. Hong, T.S. Duffy, L. Ehm, D.J. Weidner, Pressure-induced stiffness of Au nanoparticles to 71 GPa under quasi-hydrostatic loading, *J. Phys. Condens. Matter*. 27 (2015) 485303. <https://doi.org/10.1088/0953-8984/27/48/485303>.
- [27] A.S. Mikheykin, V.P. Dmitriev, S.V. Chagovets, A.B. Kuriganova, N.V. Smirnova, I.N. Leontyev, The compressibility of nanocrystalline Pt, *Appl. Phys. Lett*. 101 (2012) 173111. <https://doi.org/10.1063/1.4758000>.
- [28] B. Chen, D. Penwell, M.B. Kruger, A.F. Yue, B. Fultz, Nanocrystalline iron at high pressure, *J. Appl. Phys*. 89 (2001) 4794–4796. <https://doi.org/10.1063/1.1357780>.
- [29] Q.F. Gu, G. Krauss, F. Gramm, W. Steurer, On the compressibility of TiC in microcrystalline and nanoparticulate form, *J. Phys. Condens. Matter*. 20 (2008) 445226. <https://doi.org/10.1088/0953-8984/20/44/445226>.
- [30] Q. Wang, D. He, F. Peng, L. Xiong, J. Wang, P. Wang, C. Xu, J. Liu, Compression behavior of nanocrystalline TiN, *Solid State Commun*. 182 (2014) 26–29. <https://doi.org/10.1016/j.ssc.2013.12.015>.
- [31] D. Gerlich, G.C. Kennedy, The elastic moduli and their pressure derivatives for tungsten carbide with different amounts of cobalt binder, *J. Appl. Phys*. 50 (1979) 3331–3333. <https://doi.org/10.1063/1.326273>.
- [32] D.V. Suetin, I.R. Shein, A.L. Ivanovskii, Elastic and electronic properties of hexagonal and cubic polymorphs of tungsten monocarbide WC and mononitride WN from first-principles calculations, *Phys. Status Solidi B*. 245 (2008) 1590–1597. <https://doi.org/10.1002/pssb.200844077>.
- [33] I.R. Shein, D.V. Suetin, A.L. Ivanovskii, Elastic properties of carbide, nitride, and boride ceramics with WC-type structures, *Tech. Phys. Lett*. 34 (2008) 841–844. <https://doi.org/10.1134/S106378500810009X>.
- [34] Y.D. Su, C.Q. Hu, C. Wang, M. Wen, W.T. Zheng, Relatively low temperature synthesis of hexagonal tungsten carbide films by N doping and its effect on the preferred orientation, phase transition, and mechanical properties, *J. Vac. Sci. Technol. Vac. Surf. Films*. 27 (2009) 167–173. <https://doi.org/10.1116/1.3058721>.

- [35] L. Liu, Y. Bi, J. Xu, X. Chen, Ab initio study of the structural, elastic, and thermodynamic properties of tungsten monocarbide at high pressure and high temperature, *Phys. B Condens. Matter.* 413 (2013) 109–115. <https://doi.org/10.1016/j.physb.2012.11.026>.
- [36] X. Li, X. Zhang, J. Qin, S. Zhang, J. Ning, R. Jing, M. Ma, R. Liu, First-principles calculations of structural stability and mechanical properties of tungsten carbide under high pressure, *J. Phys. Chem. Solids.* 75 (2014) 1234–1239. <https://doi.org/10.1016/j.jpcs.2014.06.011>.
- [37] H.J. Goldschmidt, *Interstitial Alloys*, 1st ed., Butterworth & Co., Lt.d., London, UK, 1967. DOI 10.1007/978-1-4899-5880-.
- [38] A.Y. Liu, R.M. Wentzcovitch, M.L. Cohen, Structural and electronic properties of WC, *Phys. Rev. B.* 38 (1988) 9483–9489. <https://doi.org/10.1103/PhysRevB.38.9483>.
- [39] J.D. Bolton, M. Redington, Plastic deformation mechanisms in tungsten carbide, *J. Mater. Sci.* 15 (1980) 3150–3156. <https://doi.org/10.1007/BF00550388>.
- [40] T. Takahashi, E.J. Freise, Determination of the slip systems in single crystals of tungsten monocarbide, *Philos. Mag.* 12 (1965) 1–8. <https://doi.org/10.1080/14786436508224941>.
- [41] D.M. Teter, Computational Alchemy: The Search for New Superhard Materials, *MRS Bull.* 23 (1998) 22–27. <https://doi.org/10.1557/S0883769400031420>.
- [42] T. Irifune, A. Kurio, S. Sakamoto, T. Inoue, H. Sumiya, Ultrahard polycrystalline diamond from graphite, *Nature.* 421 (2003) 599. <https://doi.org/10.1038/421599b>.
- [43] H. Sumiya, S. Uesaka, S. Satoh, Mechanical properties of high purity polycrystalline cBN synthesized by direct conversion sintering method, *J. Mater. Sci.* 35 (2000) 1181–1186.
- [44] N. Dubrovinskaia, V.L. Solozhenko, N. Miyajima, V. Dmitriev, O.O. Kurakevych, L. Dubrovinsky, Superhard nanocomposite of dense polymorphs of boron nitride: Noncarbon material has reached diamond hardness, *Appl. Phys. Lett.* 90 (2007) 101912. <https://doi.org/10.1063/1.2711277>.
- [45] N.C. Popa, The (hkl) Dependence of Diffraction-Line Broadening Caused by Strain and Size for all Laue Groups in Rietveld Refinement, *J. Appl. Crystallogr.* 31 (1998) 176–180. <https://doi.org/10.1107/S0021889897009795>.
- [46] M. Rivers, V. Prakapenka, A. Kubo, C. Pullins, C. Holl, S. Jacobsen, The COMPRES/GSECARS gas-loading system for diamond anvil cells at the Advanced Photon Source, *High Press. Res.* 28 (2008) 273–292. <https://doi.org/10.1080/08957950802333593>.
- [47] R. Hrubiaik, S. Sinogeikin, E. Rod, G. Shen, The laser micro-machining system for diamond anvil cell experiments and general precision machining applications at the High Pressure Collaborative Access Team, *Rev. Sci. Instrum.* 86 (2015) 072202. <https://doi.org/10.1063/1.4926889>.
- [48] A. Dewaele, P. Loubeyre, M. Mezouar, Equations of state of six metals above 94 GPa, *Phys. Rev. B.* 70 (2004). <https://doi.org/10.1103/PhysRevB.70.094112>.
- [49] A.P. Hammersley, S.O. Svensson, M. Hanfland, A.N. Fitch, D. Hausermann, Two-dimensional detector software: From real detector to idealised image or two-theta scan, *High Press. Res.* 14 (1996) 235–248. <https://doi.org/10.1080/08957959608201408>.
- [50] C. Prescher, V.B. Prakapenka, *DIOPTAS* : a program for reduction of two-dimensional X-ray diffraction data and data exploration, *High Press. Res.* 35 (2015) 223–230. <https://doi.org/10.1080/08957959.2015.1059835>.
- [51] L. Lutterotti, S. Matthies, H.-R. Wenk, MAUD: a friendly Java program for material analysis using diffraction, *CPD News.* 21 (1999) 14–15.
- [52] L. Lutterotti, S. Matthies, H.-R. Wenk, A.S. Schultz, J.W. Richardson, Combined texture and structure analysis of deformed limestone from time-of-flight neutron diffraction spectra, *J. Appl. Phys.* 81 (1997) 594–600. <https://doi.org/10.1063/1.364220>.
- [53] D. Chateigner, L. Lutterotti, M. Morales, Quantitative texture analysis and combined analysis. Section 5.3.2.3.6. EWIMV method, in: *Int. Tables Crystallogr.*, n.d.: p. 560.

- <http://onlinelibrary.wiley.com/iucr/itc/Ha/ch5o3v0001/sec5o3o2o3o6/?> (accessed August 11, 2020).
- [54] L. Lutterotti, D. Chateigner, S. Ferrari, J. Ricote, Texture, residual stress and structural analysis of thin films using a combined X-ray analysis, *Thin Solid Films*. 450 (2004) 34–41. <https://doi.org/10.1016/j.tsf.2003.10.150>.
- [55] H.-R. Wenk, S. Matthies, J. Donovan, D. Chateigner, BEARTEX: a Windows-based program system for quantitative texture analysis, *J. Appl. Crystallogr.* 31 (1998) 262–269. <https://doi.org/10.1107/S002188989700811X>.
- [56] T.J.B. Holland, S.A.T. Redfern, Unit cell refinement from powder diffraction data: the use of regression diagnostics, *Mineral. Mag.* 61 (1997) 65–77.
- [57] H. -k. Mao, J. Xu, P.M. Bell, Calibration of the Ruby Pressure Gauge to 800 kbar Under Quasi-Hydrostatic Conditions, *J. Geophys. Res.* 91 (1986) 4673–4676. <https://doi.org/10.1029/JB091iB05p04673>.
- [58] D.L. Heinz, R. Jeanloz, The equation of state of the gold calibration standard, *J. Appl. Phys.* 55 (1984) 885–893. <https://doi.org/10.1063/1.333139>.
- [59] D.P. Dandekar, Shock Equation of State and Dynamic Strength of Tungsten Carbide, in: *AIP Conf. Proc.*, AIP, Atlanta, Georgia (USA), 2002: pp. 783–786. <https://doi.org/10.1063/1.1483654>.
- [60] T.S. Duffy, G. Shen, D.L. Heinz, J. Shu, Y. Ma, H.-K. Mao, R.J. Hemley, A.K. Singh, Lattice strains in gold and rhenium under nonhydrostatic compression to 37 GPa, *Phys. Rev. B*. 60 (1999) 15063.
- [61] A.K. Singh, H. Mao, J. Shu, R.J. Hemley, Estimation of single-crystal elastic moduli from polycrystalline X-ray diffraction at high pressure: application to FeO and iron, *Phys. Rev. Lett.* 80 (1998) 2157.
- [62] A.L. Ruoff, Stress anisotropy in opposed anvil high-pressure cells, *J. Appl. Phys.* 46 (1975) 1389. <https://doi.org/10.1063/1.321737>.
- [63] A.K. Singh, C. Balasingh, H. Mao, R.J. Hemley, J. Shu, Analysis of lattice strains measured under nonhydrostatic pressure, *J. Appl. Phys.* 83 (1998) 7567–7575. <https://doi.org/10.1063/1.367872>.
- [64] A.K. Singh, C. Balasingh, The lattice strains in a specimen (hexagonal system) compressed nonhydrostatically in an opposed anvil high pressure setup, *J. Appl. Phys.* 75 (1994) 4956–4962. <https://doi.org/10.1063/1.355786>.
- [65] A.K. Singh, The lattice strains in a specimen (cubic system) compressed nonhydrostatically in an opposed anvil device, *J. Appl. Phys.* 73 (1993) 4278. <https://doi.org/10.1063/1.352809>.
- [66] A.K. Singh, Analysis of nonhydrostatic high-pressure diffraction data (cubic system): Assessment of various assumptions in the theory, *J. Appl. Phys.* 106 (2009) 043514. <https://doi.org/10.1063/1.3197213>.
- [67] J.F. Nye, *Physical Properties of Crystals: Their Representation by Tensors and Matrices*, 2nd ed., Clarendon Press, 1985.
- [68] H.-R. Wenk, L. Lutterotti, S.C. Vogel, Rietveld texture analysis from TOF neutron diffraction data, *Powder Diffr.* 25 (2010) 283–296. <https://doi.org/10.1154/1.3479004>.
- [69] H. Wang, P.D. Wu, C.N. Tomé, Y. Huang, A finite strain elastic–viscoplastic self-consistent model for polycrystalline materials, *J. Mech. Phys. Solids*. 58 (2010) 594–612. <https://doi.org/10.1016/j.jmps.2010.01.004>.
- [70] F. Lin, N. Hilaret, P. Raterron, A. Addad, J. Immoor, H. Marquardt, C.N. Tomé, L. Miyagi, S. Merkel, Elasto-viscoplastic self consistent modeling of the ambient temperature plastic behavior of periclase deformed up to 5.4 GPa, *J. Appl. Phys.* 122 (2017) 205902. <https://doi.org/10.1063/1.4999951>.
- [71] K. Mandel, M. Radajewski, L. Krüger, Strain-rate dependence of the compressive strength of WC–Co hard metals, *Mater. Sci. Eng. A*. 612 (2014) 115–122. <https://doi.org/10.1016/j.msea.2014.06.020>.

- [72] Lin, Giannetta, Jule, Couper, Dunleavy, Miyagi, Texture Development and Stress–Strain Partitioning in Periclase + Halite Aggregates, *Minerals*. 9 (2019) 679. <https://doi.org/10.3390/min9110679>.
- [73] N.C. Popa, D. Balzar, An analytical approximation for a size-broadened profile given by the lognormal and gamma distributions, *J. Appl. Crystallogr.* 35 (2002) 338–346. <https://doi.org/10.1107/S0021889802004156>.
- [74] A.K. Singh, H.P. Liermann, S.K. Saxena, H.K. Mao, S.U. Devi, Nonhydrostatic compression of gold powder to 60 GPa in a diamond anvil cell: estimation of compressive strength from x-ray diffraction data, *J. Phys. Condens. Matter*. 18 (2006) S969. <https://doi.org/10.1088/0953-8984/18/25/S05>.
- [75] G.K. Williamson, W.H. Hall, X-ray line broadening from filed aluminium and wolfram, *Acta Metall.* 1 (1953) 22–31. [https://doi.org/10.1016/0001-6160\(53\)90006-6](https://doi.org/10.1016/0001-6160(53)90006-6).
- [76] N. Funamori, T. Yagi, T. Uchida, Deviatoric stress measurement under uniaxial compression by a powder x-ray diffraction method, *J. Appl. Phys.* 75 (1994) 4327–4331. <https://doi.org/10.1063/1.355975>.
- [77] R.J. Angel, M. Bujak, J. Zhao, G.D. Gatta, S.D. Jacobsen, Effective hydrostatic limits of pressure media for high-pressure crystallographic studies, *J. Appl. Crystallogr.* 40 (2007) 26–32. <https://doi.org/10.1107/S0021889806045523>.
- [78] S. Klotz, J.-C. Chervin, P. Munsch, G. Le Marchand, Hydrostatic limits of 11 pressure transmitting media, *J. Phys. Appl. Phys.* 42 (2009) 075413. <https://doi.org/10.1088/0022-3727/42/7/075413>.
- [79] S.M. Dorfman, V.B. Prakapenka, Y. Meng, T.S. Duffy, Intercomparison of pressure standards (Au, Pt, Mo, MgO, NaCl and Ne) to 2.5 Mbar, *J. Geophys. Res.* 117 (2012). <https://doi.org/10.1029/2012JB009292>.
- [80] D. He, S.R. Shieh, T.S. Duffy, Strength and equation of state of boron suboxide from radial x-ray diffraction in a diamond cell under nonhydrostatic compression, *Phys. Rev. B*. 70 (2004) 184121. <https://doi.org/10.1103/PhysRevB.70.184121>.
- [81] G.M. Amulele, M.H. Manghnani, M. Somayazulu, Application of radial x-ray diffraction to determine the hydrostatic equation of state and strength of TiB₂ up to 60 GPa, *J. Appl. Phys.* 99 (2006) 023522. <https://doi.org/10.1063/1.2164533>.
- [82] H. Dong, D. He, T.S. Duffy, Y. Zhao, Elastic moduli and strength of nanocrystalline cubic BC 2 N from x-ray diffraction under nonhydrostatic compression, *Phys. Rev. B*. 79 (2009) 014105. <https://doi.org/10.1103/PhysRevB.79.014105>.
- [83] H. Dong, S.M. Dorfman, Y. Chen, H. Wang, J. Wang, J. Qin, D. He, T.S. Duffy, Compressibility and strength of nanocrystalline tungsten boride under compression to 60 GPa, *J. Appl. Phys.* 111 (2012) 123514. <https://doi.org/10.1063/1.4728208>.
- [84] D.J. Weidner, L. Li, M. Davis, J. Chen, Effect of plasticity on elastic modulus measurements, *Geophys. Res. Lett.* 31 (2004) n/a-n/a. <https://doi.org/10.1029/2003GL019090>.
- [85] P. Raterron, S. Merkel, *In situ* rheological measurements at extreme pressure and temperature using synchrotron X-ray diffraction and radiography, *J. Synchrotron Radiat.* 16 (2009) 748–756. <https://doi.org/10.1107/S0909049509034426>.
- [86] S. Merkel, T. Yagi, Effect of lattice preferred orientation on lattice strains in polycrystalline materials deformed under high pressure: Application to hcp-Co, *J. Phys. Chem. Solids*. 67 (2006) 2119–2131. <https://doi.org/10.1016/j.jpcs.2006.05.025>.
- [87] S. Merkel, C. Tomé, H.-R. Wenk, Modeling analysis of the influence of plasticity on high pressure deformation of hcp-Co, *Phys. Rev. B*. 79 (2009) 064110. <https://doi.org/10.1103/PhysRevB.79.064110>.

- [88] S. Merkel, N. Miyajima, D. Antonangeli, G. Fiquet, T. Yagi, Lattice preferred orientation and stress in polycrystalline hcp-Co plastically deformed under high pressure, *J. Appl. Phys.* 100 (2006) 023510. <https://doi.org/10.1063/1.2214224>.
- [89] V.P. Zhukov, V.A. Gubanov, Energy band structure and thermo-mechanical properties of tungsten and tungsten carbides as studied by the LMTO-ASA method, *Solid State Commun.* 56 (1985) 51–55. [https://doi.org/10.1016/0038-1098\(85\)90532-0](https://doi.org/10.1016/0038-1098(85)90532-0).
- [90] M. Christensen, S. Dudiy, G. Wahnström, First-principles simulations of metal-ceramic interface adhesion: Co/WC versus Co/TiC, *Phys. Rev. B.* 65 (2002) 045408. <https://doi.org/10.1103/PhysRevB.65.045408>.
- [91] X.-S. Kong, Y.-W. You, J.H. Xia, C.S. Liu, Q.F. Fang, G.-N. Luo, Q.-Y. Huang, First principles study of intrinsic defects in hexagonal tungsten carbide, *J. Nucl. Mater.* 406 (2010) 323–329. <https://doi.org/10.1016/j.jnucmat.2010.09.002>.
- [92] X. Feng, J. Chang, Y. Lu, Experimental research on HEL and failure properties of alumina under impact loading, *Def. Technol.* 12 (2016) 272–276. <https://doi.org/10.1016/j.dt.2016.01.007>.
- [93] B. Kiefer, S.R. Shieh, T.S. Duffy, T. Sekine, Strength, elasticity, and equation of state of the nanocrystalline cubic silicon nitride γ -Si₃N₄ to 68 GPa, *Phys. Rev. B.* 72 (2005) 014102. <https://doi.org/10.1103/PhysRevB.72.014102>.